J. Fluid Mech. (2021), *vol*. 915, A4, doi:10.1017/jfm.2021.12

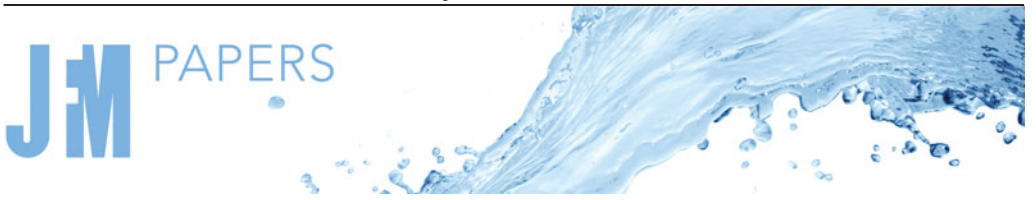

Concave-wall turbulent boundary layers without and with free-stream turbulence

Jiho You[1], **David A. Buchta**[1] **and Tamer A. Zaki**[1,†]

[1]Department of Mechanical Engineering, Johns Hopkins University, Baltimore, MD 21218, USA

(Received 17 June 2020; revised 18 December 2020; accepted 3 January 2021)

Direct numerical simulations are performed to contrast turbulent boundary layers over a concave wall without and with free-stream turbulence. An adverse pressure gradient near the onset of curvature leads to a sharp decrease in skin friction and intermittent separation. The presence of free-stream turbulence reduces the probability of reverse flow, accelerates the recovery of the boundary layer in the downstream zero-pressure-gradient region, and leads to a sustained and appreciable increase in the skin friction. The forcing also promotes the amplification of coherent Görtler structures in the logarithmic layer of the curved-wall boundary layer. Statistically, the spanwise and wall-normal Reynolds stresses intensify and the radial distance between their peaks increases downstream as the Görtler structures expand. The Reynolds shear stress coefficient also increases in the logarithmic layer, in contrast to a decrease when a flat-plate boundary layer is exposed to free-stream turbulence. In addition, the more coherent and energetic roll motions in the forced flow promote mixing of free-stream and boundary-layer fluids, where the former is seen more often deep within the buffer layer.

Key words: turbulence simulation, intermittency

1. Introduction

In practical flow configurations, turbulent boundary layers (TBLs) often develop over curved surfaces. The focus in the present study is on concave curvature, which induces centrifugal effects in addition to the external pressure gradient. Another important practical consideration is the presence of environmental disturbances, or free-stream forcing, which can appreciably alter the dynamics within the underlying boundary layer. For example, when a flat-plate TBL is buffeted by free-stream turbulence (FST), its thickness and skin-friction coefficient increase appreciably, even when the free-stream fluid has not breached the logarithmic layer (You & Zaki 2019). The present work uses direct numerical simulations (DNS) to probe the combined effects of the concave curvature

† Email address for correspondence: t.zaki@jhu.edu

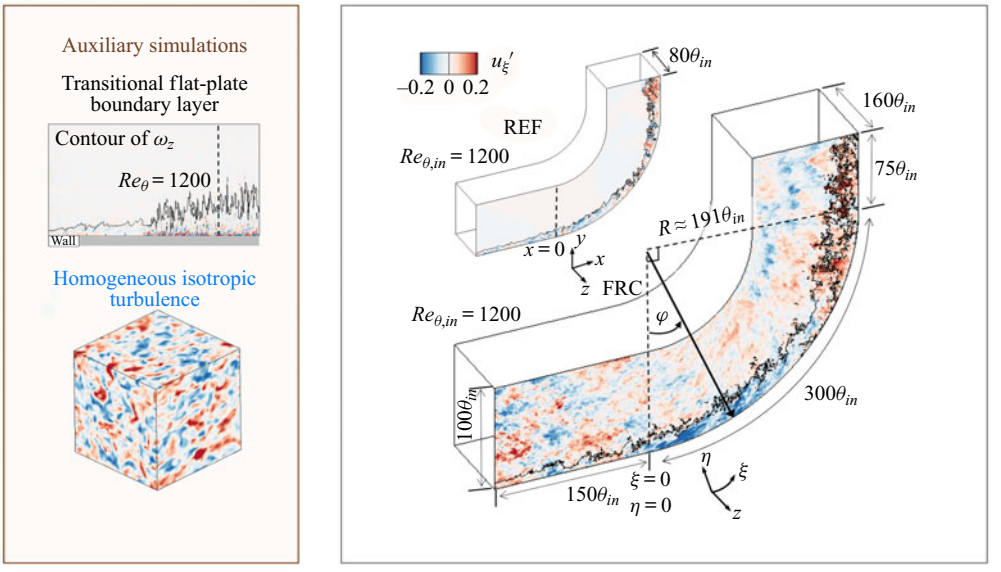

Figure 1. Configurations of two auxiliary computations to generate the inflow conditions, and the two main computations of TBL over curved wall without and with FST.

and FST on the boundary layer. Two simulations are contrasted, corresponding to the TBL on the concave wall developing beneath quiescent and vortical free streams (see figure 1).

1.1. *TBL on concave wall*

Curved-wall TBLs are influenced by three effects (Floryan 1991): (i) turbulence changes due to the mean-flow turning, (ii) potential formation of coherent Görtler vortices and (iii) the impact of these coherent vortices on the turbulence. The second mechanism is triggered when the boundary-layer thickness (e.g. momentum thickness θ) is comparable to the radius of curvature (R). In laminar flows, an instability, due to the gradient of angular momentum in the radial direction, leads to the formation of longitudinal Görtler vortices (Saric 1994; Schrader, Brandt & Zaki 2011). In turbulent flows, however, Görtler structures are notoriously difficult to identify, which impedes precise description. The complexity is compounded when TBLs are exposed to FST: whether the external forcing will decorrelate the structures or enhance them is uncertain, and how the coupling between the Görtler structures and the finer-scale boundary-layer turbulence will be affected is unknown.

Much of the literature on curved-wall turbulence has focused on conditions with quiescent free streams. Barlow & Johnston (1988*a*) performed experiments to probe the response of the boundary layer to a sudden onset of concave curvature. They reported that higher-momentum eddies move towards the wall, while lower-momentum eddies travel away from it. Despite efforts to visualize the streamwise vortices using the coloured-dye and laser-induced-fluorescence methods, direct observation of Görtler vortices was difficult; yet enhanced shear stress in the outer boundary layer region suggests their presence. In other works, Hoffmann, Muck & Bradshaw (1985) and Barlow & Johnston (1988*b*) used a vortex generator to induce large-scale, time-stable roll cells, which produced a coupling between the large-scale outer fluid motions and near-wall turbulence. Barlow & Johnston (1988*b*) showed that the downwash suppresses the bursting, which induces interactions between sublayer structures and outer-layer eddies, while the upwash

enhances the process. However, the connection between naturally occurring Görtler vortices in turbulence (irregularly spaced and temporally intermittent) and those produced by synthetic means is unknown (e.g. Patel & Sotiropoulos 1997).

Lund & Moin (1996) and Arolla & Durbin (2015) numerically modelled the experiment by Barlow & Johnston (1988*a*). They used large-eddy simulations to directly probe the longitudinal vortices due to the centrifugal effect. Spatially filtering the turbulence field revealed streamwise-aligned structures inside the TBL above the curved wall, which supports the existence of Görtler structures within the boundary-layer turbulence (Lund & Moin 1996; Arolla & Durbin 2015). However, the degree to which the external pressure gradient influences the TBL on the curved surface – an effect that depends on the flow set-up – was not addressed. At the onset of mean-streamline curvature, an adverse pressure gradient (APG) is established, and the opposite effect takes place at the end of the curved section. Top walls can be contoured to isolate curvature effects from the streamwise pressure gradient (Barlow & Johnston 1988*a*,*b*), but in practical configurations the pressure gradient is present and impacts the behaviour of the flow on the curved wall.

A related configuration is the flow in an S-shaped duct, where the boundary layer is subject to pressure gradients and curvature. Experiments show that the skin friction has local extrema after curvature changes, which are concomitant with streamwise pressure variations (Bandyopadhyay & Ahmed 1993). Corresponding large-eddy simulations by Lopes, Piomelli & Palma (2006) show that the mean flow was separated near the convex-to-concave transition due to the strong APG. Intermittent separation was also observed as the flow progressed from the convex to the flat region, but the phenomenon was seldom observed in the flat-to-concave transition (Lopes *et al.* 2006).

Studies that have examined FST–TBL interactions over curved walls have mainly focused on the flow recovery from the curved section on the downstream flat wall. Kestoras & Simon (1995) compared the boundary layers at low and high inlet FST intensities, $Tu = 0.6\,\%$ and $Tu = 8\,\%$, and reported an increase in skin friction of up to $20\,\%$ in the latter case. The authors also contrasted their ability to identify the Görtler vortices on the curved section at low turbulence intensity with their inability to do so at the higher Tu, which is at odds with the currently accepted view that free-stream forcing promotes the generation of outer large-scale motions in wall turbulence (e.g. You & Zaki 2019). In the same experimental configuration, Kestoras & Simon (1998) used the temperature field over the constant-heat-flux plate to evaluate the probability of observing boundary-layer fluid, which was their definition of intermittency. The forced case exhibited enhanced mixing, a trend that is in agreement with observations of flat-plate boundary layers exposed to FST (Hancock & Bradshaw 1989). Their intermittency curves, however, were not presented in viscous scaling, so it is not possible to quantify the extent to which the free-stream fluid penetrated towards the wall.

1.2. *Effects of FST on flat-plate TBLs*

The influence of FST on TBL has much more commonly been studied in zero-pressure-gradient (ZPG), flat-plate boundary layers. Early experiments were performed using grid-generated FST with intensities $Tu \lesssim 7\,\%$ (Simonich & Bradshaw 1978; Hancock & Bradshaw 1983, 1989; Castro 1984). Simonich & Bradshaw (1978) reported that the drag and also the heat-transfer rate increase proportionally to Tu. Hancock & Bradshaw (1983) demonstrated a marked effect of the FST length scale on TBL response. They introduced the non-dimensional parameter $b \equiv Tu(\%)/(L_u/\delta + 2)$, where L_u and δ are the dissipation length scale and boundary layer thickness, and showed

that skin friction increases with b. Hancock & Bradshaw (1989) thermally 'tagged' the boundary-layer fluid in order to perform conditional sampling. They reported that FST increases the standard deviation of the intermittency profiles, and that the isotropy of FST reduces the Reynolds-shear-stress correlation coefficient in the boundary layer. Ames & Moffat (1990) and Thole & Bogard (1995, 1996) investigated the influence of higher free-stream intensities $Tu \gtrsim 10\,\%$. The former effort reported that under these intense conditions, skin friction depends not only on b, but also on the Reynolds number. In contrast, Thole & Bogard (1995) affirmed that skin friction depends mainly on b, up to the turbulent intensity $Tu = 28\,\%$. Based on simulations of forced temporal boundary layers, Kozul *et al.* (2020) reported that another relevant parameter is the ratio of eddy-turnover timescales of the FST and boundary layer. Too small a value leads to weak interactions since the external turbulence decays quickly and cannot influence the boundary layer.

The changes in the spectra and flow structures in the boundary layer, when exposed to free-stream forcing, are noteworthy. Absent free-stream disturbances, a peak in the pre-multiplied energy spectra in the outer part of the boundary layer signals the formation of large-scale motions (Hutchins & Marusic 2007; Mathis, Hutchins & Marusic 2009) – a behaviour that is observed at Reynolds numbers $Re_\tau \geq 2000$. Under the influence of FST, that outer peak is observed at lower Reynolds numbers, in both the streamwise and spanwise energy spectra (Thole & Bogard 1996; You & Zaki 2019).

FST forcing also leads to an increase in the near-wall streamwise velocity fluctuations. Using a scale-decomposition analysis, Dogan, Hanson & Ganapathisubramani (2016) attributed this increase to large scales relative to a cut-off wavelength between 1 and 2δ. Hearst, Dogan & Ganapathisubramani (2018) divided the spectrogram of the streamwise velocity fluctuations into four regions based on the wall-normal height and wavelength. Near the wall, the large-wavelength region is significantly affected by the FST, although the small-scale inner peak was relatively insensitive to external forcing. Based on these results, Hearst *et al.* (2018) concluded that the FST is directly observed in the near-wall region.

The recent DNS of You & Zaki (2019, 2020) provided a detailed analysis of the interaction of FST with underlying flat-plate boundary layers at Reynolds numbers exceeding $Re_\theta \simeq 3200$. A level-set approach was embedded in the simulations to objectively distinguish the free-stream and boundary-layer fluids, and to quantify the degree of penetration of the former into the latter (and vice versa). The level-set approach thus provided an unambiguous description of the respective roles of the free-stream and boundary-layer turbulence, and their respective contributions to observations through conditional sampling. The results showed that only the low-frequency component of the FST penetrates the logarithmic layer, which is consistent with the phenomenon of shear sheltering (Hunt & Durbin 1999; Zaki & Saha 2009). The outcomes are a direct increase in the turbulence kinetic energy (TKE) in this region, and the formation of large-scale motions at lower Reynolds numbers than in canonical unforced boundary layers. In contrast to the logarithmic region, the FST did not directly reach the buffer layer, and the increase in the near-wall TKE was due to an indirect effect: the formation and amplification of the outer large-scale motions modulated the near-wall structures and led to the increase in their TKE.

In contrast to the recent discoveries in the context of FST interactions with flat-plate boundary layers, much less is known regarding how such interaction unfolds on curved walls. The present work will highlight that FST has important implications as early as the onset of curvature where the flow experiences an APG, which can lead to intermittent separation. The external forcing also appreciably alters the boundary-layer statistics and

the Görtler structures on the curved section and has important practical implications for the wall stress. We perform two simulations: (i) a reference case with a quiescent free stream and (ii) a forced case with 10 % FST intensity at the inlet plane. The set-up of the simulations is described in § 2. Key statistical results are presented in § 3 and changes to boundary-layer structures are discussed in § 4. The conclusions are provided in the final section.

2. Simulation set-up

The flow configuration adopted in the present study is shown in figure 1. The flow is governed by the incompressible Navier–Stokes and continuity equations, which, expressed in non-dimensional form, are

$$\frac{\partial u_i}{\partial t} + \frac{\partial u_i u_j}{\partial x_j} = -\frac{\partial p}{\partial x_i} + \frac{1}{Re_{\theta_{in}}}\frac{\partial^2 u_i}{\partial x_j^2}, \tag{2.1}$$

$$\frac{\partial u_j}{\partial x_j} = 0. \tag{2.2}$$

The reference scales are the free-stream velocity U_∞ and the boundary-layer momentum thickness θ_{in} at the inflow of the main simulation domain. The momentum-thickness Reynolds number at the inflow is $Re_{\theta_{in}} \equiv \rho U_\infty \theta_{in}/\mu = 1200$, where ρ and μ are the density and dynamic viscosity, respectively. The velocity components in the streamwise (ξ), wall-normal (η) and spanwise (z) directions are u_ξ, u_η and w, respectively, and the pressure is p. Note that x and y indicate the horizontal and vertical Cartesian coordinates.

The flow equations are solved using a fractional step algorithm on a staggered grid with a local volume-flux formulation (Rosenfeld, Kwak & Vinokur 1991). The algorithm was extensively validated and adopted in DNS of transitional (Zaki *et al.* 2010; Schrader *et al.* 2011) and turbulent flows (Jelly, Jung & Zaki 2014; Wang, Wang & Zaki 2019). The viscous terms are integrated in time using the implicit Crank–Nicolson method, and the convective terms are treated explicitly using the Adams–Bashforth scheme. The pressure equation is solved using Fourier transform in the periodic spanwise direction and geometric multigrid for the resulting Helmholtz equation, then used to project the intermediate velocity onto a divergence-free field.

Two main simulations are contrasted: a reference (REF) case where the curved-wall boundary layer develops beneath a quiescent free stream and a forced (FRC) case where the free stream is turbulent. In both cases, the flow domains include an initial flat section ($150\theta_{in}$), a curved section ($300\theta_{in}$) and a recovery flat section ($75\theta_{in}$). The quarter-circular section has radius $R = 191\theta_{in}$. The spanwise domain of the forced configuration is twice as large as that of the reference case, in order to accommodate the formation of the large-scale structures which are anticipated based on earlier studies (You & Zaki 2019). In addition, the spanwise two-point velocity correlations have been evaluated to confirm that the widths of the domains are sufficiently large. Table 1 summarizes the domain sizes and grid resolutions. The grids are uniform in the span and stretched in the wall-normal direction using a hyperbolic tangent function. In the streamwise direction, the grid spacing is uniform on the bottom wall ($\eta = 0$). On the top surface, the grid is uniform on the curved section and is adjusted smoothly near the changes in curvature. An elliptic grid generation technique (e.g. Thompson, Warsi & Mastin 1985) is adopted to reduce strong variations in mesh spacing in those regions; the ratio of successive streamwise grid spacing is less than 3 %.

Designation	Inflow	Domain size (θ_{in}) $L_\xi \times L_\eta \times L_z$	No. of grid points $N_\xi \times N_\eta \times N_z$	Resolution $\Delta\xi^+, \Delta\eta^+, \Delta z^+, \Delta t^+$
REF	TBL	$525 \times 100 \times 80$	$2688 \times 896 \times 768$	10.5, 0.29–7.8, 5.6, 0.048
FRC	TBL+HIT	$525 \times 100 \times 160$	$2688 \times 896 \times 1536$	10.5, 0.29–7.8, 5.6, 0.041

Table 1. Computational domain sizes, and spatial and temporal resolutions at the inflow plane expressed in viscous '+' units.

No-slip conditions are applied at the bottom wall, while impermeability and no-stress conditions are imposed at the parallel top boundary. The domains are periodic in the spanwise direction, and convective outflow conditions are imposed at the exit planes. In order to seed the inflow TBL and FST in the main computations, two auxiliary simulations are performed; their full details are provided in You & Zaki (2019). The first auxiliary simulation is an independent DNS of the transitional flat-plate boundary layer, where a cross-flow plane is stored in the fully turbulent regime at $Re_\theta = 1200$ as a function of time; the same data have been used for inflow conditions in a number of studies of TBL (Lee, Sung & Zaki 2017; Motoori & Goto 2019; You & Zaki 2019). The second auxiliary simulation is a pseudo-spectral DNS of homogeneous isotropic turbulence (HIT) in a periodic domain with dimensions $\{L_\xi, L_\eta, L_z\}_{HIT} = \{80, 80, 160\}$, which generates the FST. The inflow HIT has intensity $Tu = 0.1$ and length scale $L_k \equiv k^{3/2}/\epsilon \approx 10.8$, where k is the TKE and ϵ is the dissipation rate.

At the inflow plane of the main computations, either the time-dependent TBL is applied alone (REF case), or it is superposed with FST (FRC case). In the latter case, the HIT box is introduced above the edge of the boundary layer, which was identified using a normalized vorticity threshold, $(|\boldsymbol{\omega}|/(u_\tau^2/\nu))\sqrt{\delta_{99}^+} = 0.2$, where $\boldsymbol{\omega}$ is the vorticity, u_τ is the friction velocity, ν is the kinematic viscosity and δ_{99}^+ is the 99 % boundary-layer thickness in wall units (Lee *et al.* 2017). A level-set function ψ is defined at the inflow plane and tags, or differentiates, the fluid within the boundary layer ($\psi = 1$) and the free stream ($\psi = 0$). The transport equation of ψ is

$$\frac{\partial \psi}{\partial t} + \frac{\partial u_j \psi}{\partial x_j} = 0, \tag{2.3}$$

and therefore ψ is a diffusion-free scalar that serves as a virtual sharp interface between the two fluids; full details of the implementation and exhaustive validation are provided elsewhere (Jung & Zaki 2015; You & Zaki 2019). The value $\psi = 0.5$ is adopted as the threshold for conditional sampling of the boundary-layer $\psi > 0.5$ and free-stream $\psi < 0$ fluids. Note that the interface height $\eta_I = \eta(\psi = 0.5)$ provides an objective measure of the boundary-layer thickness that is less sensitive to the details of the profile than the conventional 99 % thickness.

Beyond an initial transient and once the flow over the curved surface has reached a statistically stationary state, statistics are collected for $T_{stat} = 1207.5$ (REF) and $T_{stat} = 892.5$ (FRC) convective time units. A bar will indicate an average in homogeneous coordinates, and a prime will indicate perturbation quantities according to Reynolds decomposition; for example $u_\xi = \overline{u_\xi} + u'_\xi$.

Unlike flat-plate boundary layers, the tangential free-stream velocity on the curved section is not uniform. Instead, it increases linearly outside the boundary-layer edge.

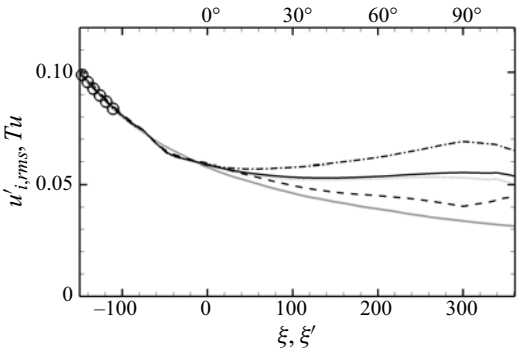

Figure 2. Downstream dependence of FST intensity Tu (black solid line), $u'_{\xi,rms}$ (black dashed line), $u'_{\eta,rms}$ (black dash-dotted line), w'_{rms} (black dotted line) and the temporal evolution of Tu (◯) in decaying HIT, which exploits the coordinate transformation $\xi' = U_\infty t$. Grey line indicates the evolution of Tu on the flat plate (You & Zaki 2019).

That potential velocity profile is denoted by U_p, and is linearly extended into the boundary layer to determine the wall value U_{pw} (Barlow & Johnston 1988*a*). The free-stream mean velocity profile influences the development of the FST as we quantify in figure 2. Upstream, within the flat section ($\xi \lesssim -100$), the decay in space in the main simulation agrees with the temporal decay of Tu in the pseudo-spectral auxiliary DNS of HIT to within the Taylor's hypothesis $\xi^* = U_\infty t$. In that region, the present results also agree with the previous study of FST over a flat-plate boundary layer (You & Zaki 2019), but the two curves show the first signs of dissimilarity ahead of the flat-to-curved transition due to the pressure gradient in that region. Farther downstream, on the curved section, the difference is more pronounced because both the mean shear in the free stream and the strain due to curvature lead to production of Reynolds shear stress, which in turn leads to production of tangential and wall-normal stresses. The outcomes are anisotropy and slower decay of the FST relative to flow over a flat plate.

Besides the FST input, the wall geometry induces a pressure gradient responsible for turning the oncoming flow, which has profound implications for boundary layer dynamics. Figure 3 shows the streamwise pressure gradient $\partial\bar{p}/\partial\xi$, the Clauser parameter $\beta = (\delta^\star/\overline{\tau_w})(\partial\bar{p}_e/\partial\xi)$ and the wall-pressure coefficient $C_{pw} \equiv (\bar{p}_{\xi,\eta=0} - \bar{p}_{\xi=0,\eta=0})/((\rho U_\infty^2)/2)$. In the definition of the Clauser parameter, $\delta^\star$ is the displacement thickness, $\overline{\tau_w}$ is the mean wall shear stress and $\bar{p}_e$ is the mean pressure at $\eta = \delta^\star$. Three regions can be clearly delineated: an approximately ZPG boundary layer on the flat plate (Region 0), APG flow near the onset of the curvature (Region 1) and nearly ZPG flow on the concave curve (Region 2). Table 2 provides information on stations which will be discussed in the following section. Region 0 has been the focus of numerous previous studies of the boundary-layer response to external turbulence (Hancock & Bradshaw 1989; Dogan *et al.* 2016; You & Zaki 2019), and hence the focus herein is directed to Region 1 and Region 2.

3. Influence of FST on the boundary layer: a statistical perspective

The present simulations involve the combined effects of pressure gradient, curvature and FST on the boundary layer. The outcome is complex, as expected. In this section, we examine the overall changes in the statistical state of the flow.

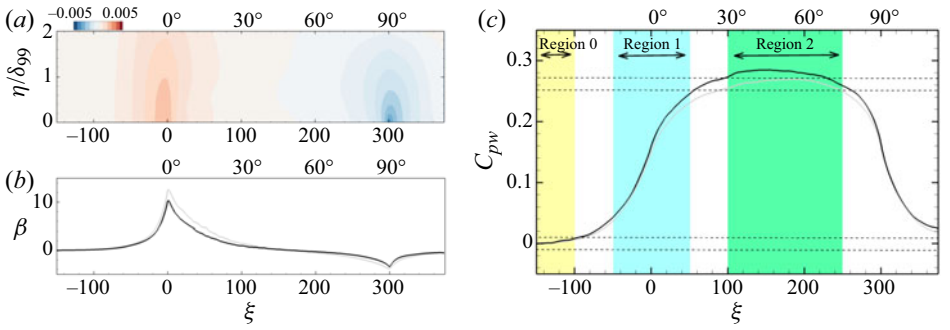

Figure 3. (*a*) Streamwise pressure gradient $\partial\bar{p}/\partial\xi$ in REF. (*b*) Clauser pressure-gradient parameter β: REF (grey) and FRC (black). (*c*) Wall-pressure coefficient, C_{pw}: REF (grey) and FRC (black). Bottom dashed lines indicate ZPG region according to the criterion of Harun *et al.* (2013), and top dashed lines mark $C_{pw,max} - C_{pw} \leq 0.02$ for REF.

Zone	Description	ξ	φ	$Re_{\tau,REF}$	$Re_{\tau,FRC}$
Region 0	ZPG on flat plate	−100	—	455	480
Region 1	APG near onset of curvature	0	0°	363	463
		+50	15°	461	623
Region 2	ZPG on concave curvature	+100	30°	557	769
		+200	60°	762	1027

Table 2. Summary of main analysis locations selected based on C_{pw} in figure 3.

FST is known to enhance mixing near the edge of the boundary layer and as a result to increase its thickness. Figure 4(*a*) reports two quantities that examine this effect: (i) $\overline{\eta_I} = \overline{\eta(\psi = 0.5)}$, which is the mean height of the virtual interface that distinguishes the boundary layer and the free stream using the level-set function, and (ii) the 99 % thickness δ_{99}, defined as the wall-normal location where $\overline{u_\xi} = 0.99U_p$. Both thickness metrics increase appreciably near the onset of the curvature due to the APG. However, over the curve in Region 2, the mean height of the material line $\overline{\eta_I}$ has a depressed growth relative to δ_{99} which is known to be sensitive to details of the mean-velocity profile. Since $\overline{\eta_I}$ has a physical interpretation, it will be adopted when possible in the rest of this work. The ratio of the boundary-layer thickness to the radius of the curved wall is $\overline{\eta_I}/R < 0.13$ (and $\delta_{99}/R < 0.17$), which places the present flows in the regime of moderate-curvature effects according to the criterion of Patel & Sotiropoulos (1997).

The root-mean-square fluctuations in the interface height η'_{rms} and its normalized value $\eta'_{rms}/\bar{\eta}_I$ are reported in figure 4(*b*). For canonical, unforced flat-plate boundary layers $\eta'_{rms}/\bar{\eta}_I$ is nearly constant. The present results demonstrate that curvature alone (grey curve, $\xi \gtrsim 50$) promotes the undulation of the interface so that $\eta'_{rms}/\bar{\eta}_I$ increases along the curved section. We therefore expect deep excursions of the free-stream fluid into the boundary layer and vice-versa along the curved section, and FST (black curves) enhances this effect. This view will be reinforced in § 4, where we directly compute intermittency.

The downstream dependence of the friction Reynolds numbers, $Re_\tau \equiv u_\tau \overline{\eta_I}/\nu$ and $Re^b_\tau \equiv u_\tau \delta_{99}/\nu$, is plotted in figure 5(*a*). Even though $\overline{\eta_I}$ and δ_{99} increase rapidly near the onset of the curvature, the APG decreases u_τ and the Reynolds numbers. The higher values

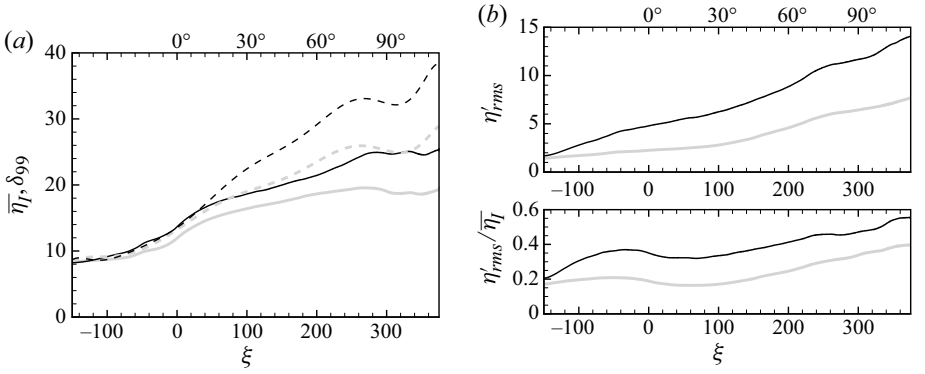

Figure 4. (*a*) Downstream development of the boundary-layer thickness δ_{99} (dashed line) and mean interface height $\overline{\eta_I}$ (solid line) based on level-set function $\psi = 0.5$. (*b*) Downstream development of the root-mean-square fluctuations in the interface height η'_{rms} and its normalized value $\eta'_{rms}/\overline{\eta_I}$: REF (grey) and FRC (black).

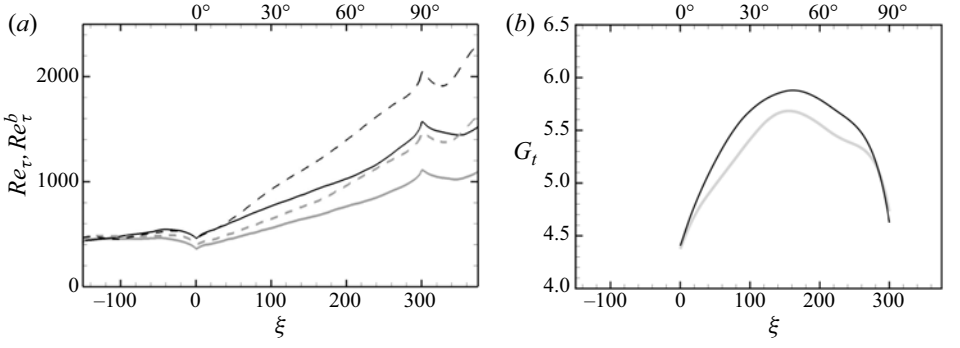

Figure 5. Downstream dependence of (*a*) the friction Reynolds numbers $Re_\tau \equiv u_\tau \overline{\eta_I}/\nu$ (solid line) and $Re^b_\tau \equiv u_\tau \delta_{99}/\nu$ (dashed line), and (*b*) the Görtler number $G_t = 43\sqrt{\theta/R}$ (Tani 1962): REF (grey) and FRC (black).

of Re_τ recorded in the FRC case are due in part to the larger boundary-layer thickness, and also to an increase in the wall stress in the presence of FST. Figure 5(*b*) shows the behaviour of the Görtler number for the TBLs,

$$G_t = \frac{U_\infty \theta}{\nu_T}\sqrt{\frac{\theta}{R}} = 43\sqrt{\frac{\theta}{R}}, \tag{3.1}$$

which uses an eddy viscosity $\nu_T = 0.0234 U_\infty \theta$ (Tani 1962). The definition of the momentum thickness θ for curved-wall flow and associated discussion are provided in appendix A. Near the onset of curvature, the Görtler number is $G_t \gtrsim 4$, which is large enough to promote instability (Smith 1955; Tani 1962), and it is larger in the FRC case. Based on this metric, FST enhances the curvature effects.

Much of the interest in concave-wall boundary layers beneath vortical forcing has been dedicated to the impact on skin friction (Kestoras & Simon 1995, 1998). The probability density function (p.d.f.) of the skin-friction coefficient, $c_f \equiv \tau_w/((\rho U^2_\infty)/2)$, is reported in figure 6, for both REF (*a*i) and FRC (*a*ii). The latter case has a broader p.d.f. which is skewed towards intense $c_f > 0$ and, as a result, has a larger mean value C_f. The largest relative increase in C_f when the flow is forced is on the order of 49 %, which is appreciably

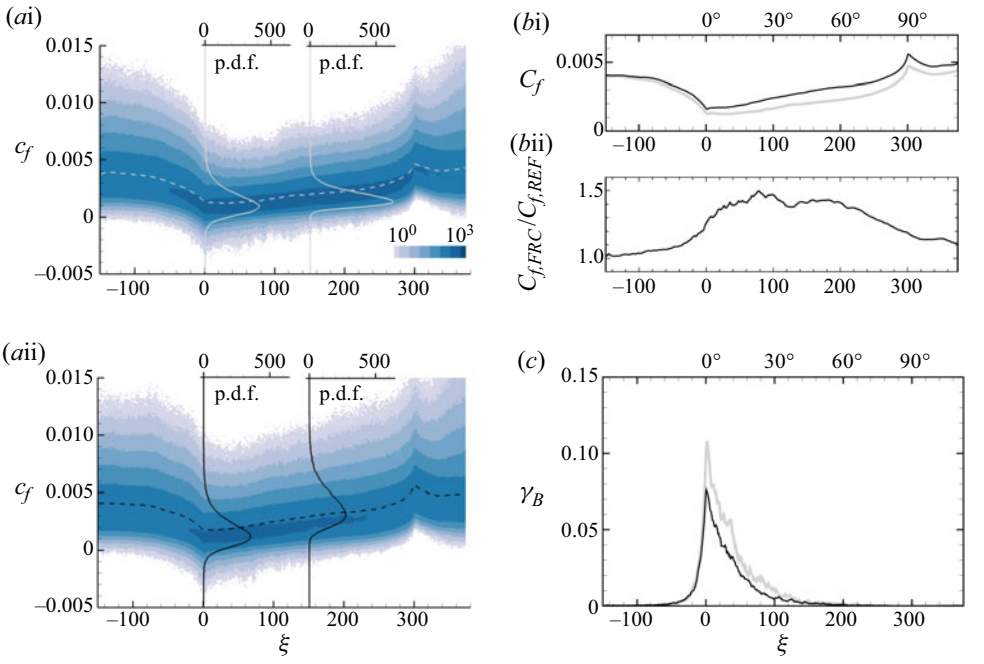

Figure 6. (*a*) Streamwise development of the p.d.f. of the instantaneous skin-friction coefficient c_f, in (i) REF and (ii) FRC. Dashed lines give the mean values, and solid lines are the p.d.f. at $\xi = 0$ and $\xi = 150$. (*b*) Downstream dependence of (i) the mean skin-friction coefficient C_f and (ii) $C_{f,FRC}/C_{f,REF}$. (*c*) Intermittency of backward flow, γ_B: REF (grey) and FRC (black).

higher than the 15 % observed for the same flow conditions over a flat plate (You & Zaki 2019). Note that the increase is not limited to the low-C_f region near the onset of curvature; instead it is sustained above 40 % over most of Region 2 on the curved wall. While the effect of forcing appears relatively modest at the onset of curvature, an important change in the state of the flow takes place in that region due to the flow deceleration. As the curvature is approached, the skin friction drops precipitously due to the APG in both the REF and the FRC case. In the latter, FST enhances momentum mixing, which leads to a more moderate reduction of C_f. The positive values of mean C_f should not, however, mask the intermittent separation clearly captured by $c_f < 0$ events in figure 6(*a*). The intermittency, or probability, of negative instantaneous wall-shear stress is denoted by γ_B and is plotted in figure 6(*c*); its reduced value in FRC is noteworthy due to the qualitative change in boundary layers at separation.

An elegant interpretation of separation is in terms of the spanwise vorticity and its wall flux; the latter is due to the streamwise pressure gradient (Lighthill 1963). Figure 7(*a*) shows the spanwise vorticity distribution near the wall. At the onset of curvature, the depletion of negative vorticity is less pronounced in the FRC case, which can be interpreted in terms of a reduction in its mean outflux at the wall. A more detailed view is provided in figure 7(*b*) which reports the p.d.f. of instantaneous outflux of negative vorticity at the onset of curvature. The integral of the p.d.f. yields a smaller value for the FRC case, consistent with figure 7(*a*). The p.d.f. of the forced case also has larger positive and negative tails, i.e. stronger instantaneous outflux of negative vorticity (positive values) and also influx (negative values). The former alone would be at odds with reduced frequency of separation. However, the strong influx of negative vorticity (negative values) renders

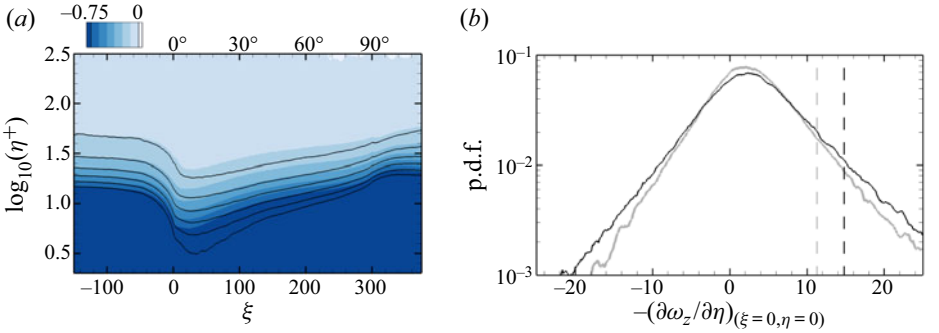

Figure 7. (*a*) Mean spanwise vorticity $-0.75 \leq \overline{\omega_z} \leq 0$ of REF (lines) and FRC (colour) cases. (*b*) P.d.f. of $-\partial\omega_z/\partial\eta$ at the wall at the onset of curvature, $(\xi, \eta) = (0, 0)$. Dashed lines mark thresholds for higher-amplitude events having the same probability as intermittent separation. Grey denotes REF; black denotes FRC.

the state of the boundary layer less prone to separation. Intuition may suggest that this effect is associated with enhanced momentum mixing on the flat upstream section, due to the additional vortical motions from the free stream that may breach the boundary layer. However, recent results for flat-plate flows have shown that FST does not reach the buffer layer within such a short streamwise distance. Instead, the external forcing has an indirect effect of modulation of the near-wall region that enhances the near-wall turbulent shear stresses (You & Zaki 2019). The resulting energetic near-wall flow is then less prone to separation at the onset of curvature. Two vertical lines are marked on figure 7(*b*); events with higher amplitudes than these thresholds have the same probability as separation (9.73 % for REF and 7.39 % for FRC). Based on this simple conceptual model, the results indicate that the threshold required for the forced boundary layer to undergo local intermittent separation is approximately 30% higher than for REF. The mean-flow profile $\overline{u_\xi}$ is therefore anticipated to be fuller in the forced flow, and is shown in figure 8. Indeed, at $\xi = 0$ through $\xi = 50$, the near-wall region of the FRC boundary layer carries more momentum than that of the reference case.

The change in the mean profile as the flow traverses from the APG Region 1 to the ZPG Region 2 on the curve is noteworthy (figure 8): the figure shows that the mean shear in (*b*ii) is slightly reduced in the outer portion of the boundary layer and the mean profile becomes fuller, which is indicative of enhanced mixing due to the FST.

Evidence of persistent, or statistically relevant, Görtler structures is sought by plotting the turbulence stresses in figure 9(*a*,*b*), for both the quiescent and turbulent free stream cases. The colour contours show the tangential component, and the lines show the wall-normal (black) and spanwise (grey) ones. The first observation is a sudden change in the contours of $\overline{u'_\xi u'_\xi}$ across the onset of curvature: the upstream wall-normal profile of $\overline{u'_\xi u'_\xi}$ has only one maximum in the buffer layer, but beyond $\xi = 0$ two maxima can be detected. The inner peak retains its original height within the buffer layer $\eta^+ \approx 11$, decays quickly due to APG and shows faster recovery in the forced flow; in contrast, the outer peak is in the logarithmic layer and shifts away from the wall with the downstream growth of the boundary layer. The emergence of the outer peak at the onset of curvature is consistent with APG (see e.g. Hickel & Adams 2008), which is sufficiently large to induce intermittent separation. In addition, relative to the reference case, FST enhances

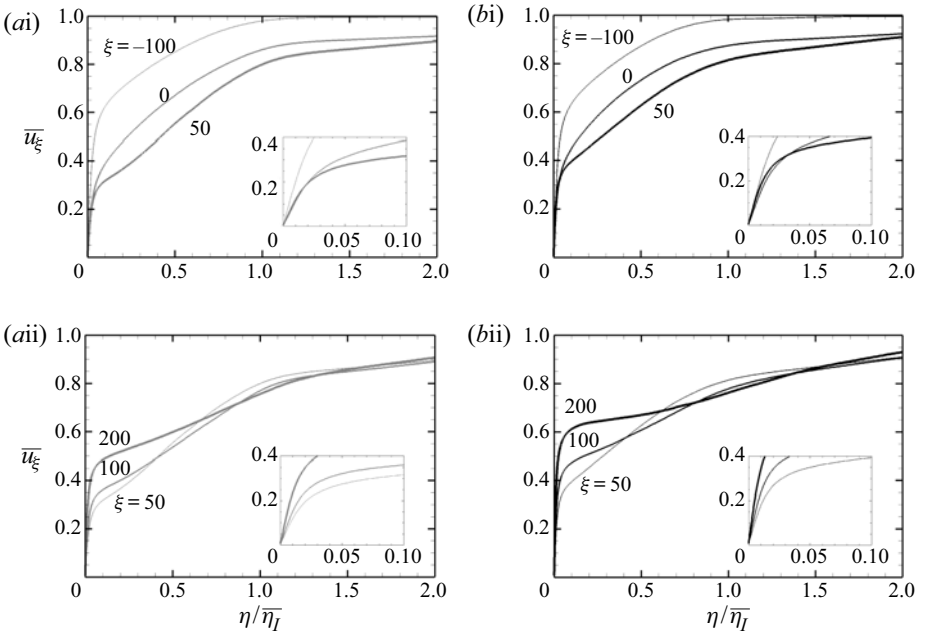

Figure 8. Downstream development of the mean streamwise velocity in (*a*) REF and (*b*) FRC. Progression (i) from the flat-plate ZPG Region 0 to APG Region 1, and (ii) from APG Region 1 to ZPG Region 2 along the curve.

the intensity of these structures – an effect that is anticipated based on previous studies of forced flat-plate boundary layers.

Observations in connection with the tangential stress are not, however, the most important to note from this figure if one's interest is in the Görtler structures. Instead, attention should be drawn to the wall-normal stress $\overline{u'_\eta u'_\eta}$ and spanwise stress $\overline{w'w'}$ in Region 2. Both stresses amplify on the curved wall, which is consistent with earlier studies (Barlow & Johnston 1988*a*; Lund & Moin 1996; Arolla & Durbin 2015), and the present results show that the effect of free-stream forcing is rather pronounced. In the lower panels (*a*ii and *b*ii), the wall-normal coordinate is normalized by the inlet boundary-layer momentum thickness, which highlights that the separation between the peaks of $\overline{u'_\eta u'_\eta}$ and $\overline{w'w'}$ increases downstream. We interpret the increase in $\overline{u'_\eta u'_\eta}$ and $\overline{w'w'}$ as the first, perhaps indirect evidence of Görtler structures (further evidence is provided in § 4). In reality, instantaneous structures may form at various heights in the boundary layer, and may meander, decay or be overtaken by other structures. For these reasons, in the statistical interpretation, we regard the peaks of $\overline{u'_\eta u'_\eta}$ and $\overline{w'w'}$ as only indicative of the locations of the Görtler structures, and hence the separation distance $d = \arg\max[\overline{u'_\eta u'_\eta}(\eta)] - \arg\max[\overline{w'w'}(\eta)]$ between their peaks as indicative of the size of the vortices (see figures 9*a*ii and 9*b*ii). Figure 10 shows the increase of the size d with downstream distance, which is greater in the forced flow in light of the stronger amplification of the outer large-scale structures and the faster growth of the boundary layer.

The departure from isotropy $I = \overline{u'_\xi u'_\xi}/2k - 1/3$ succinctly captures the changes of the perturbation field within the boundary layer, across the onset of curvature and on the

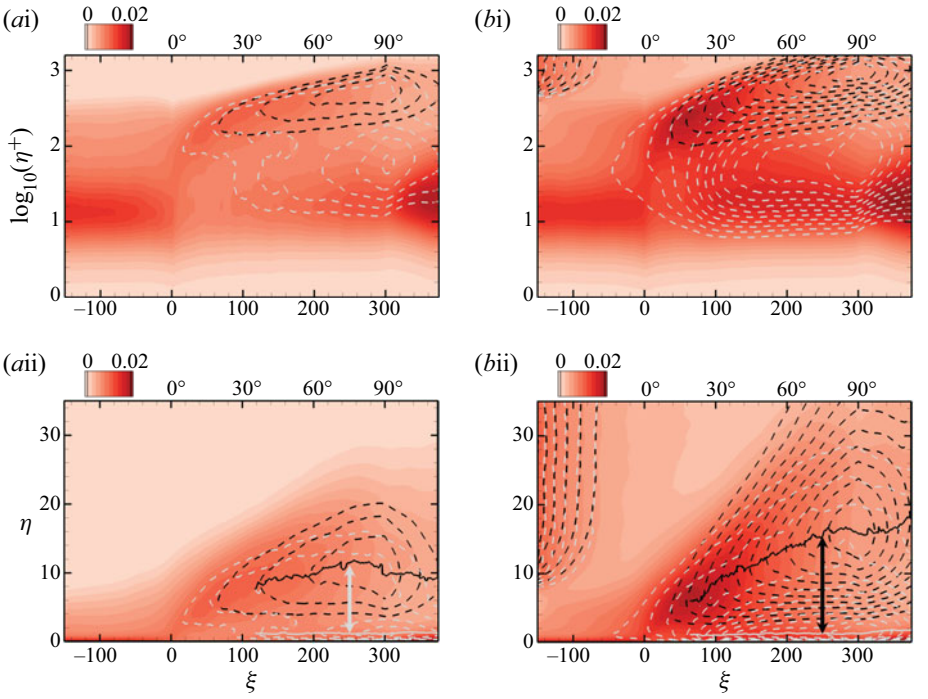

Figure 9. Reynolds normal stresses for (*a*) REF and (*b*) FRC. The wall-normal coordinate is normalized using (i) viscous and (ii) outer scales. Colours correspond to the streamwise stress, and lines show the wall-normal stress $\overline{u'_\eta u'_\eta}$ (black) and spanwise stress $\overline{w'w'}$ (grey), from 5×10^{-3} with increment 1×10^{-3}.

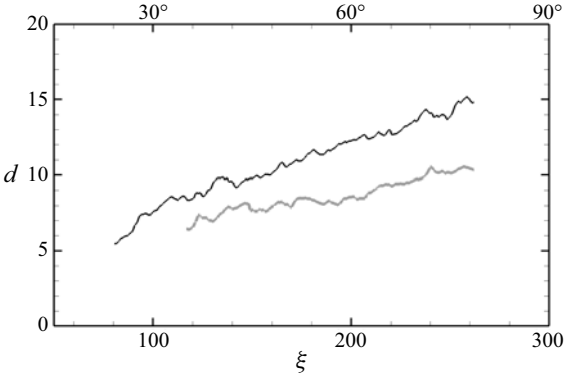

Figure 10. Separation distance d between the peaks of $\overline{u'_\eta u'_\eta}$ and $\overline{w'w'}$: REF (grey) and FRC (black).

curved wall. Figure 11 shows positive values of I in the initial flat section, which are consistent with the streamwise Reynolds stress being dominant in flat-plate boundary layers. Note that near the boundary layer edge, figure 11(*b*) shows that mixing with isotropic FST reduces I. At the onset of curvature, the appreciable increase in I reflects the increase in $\overline{u'_\xi u'_\xi}$ in the logarithmic layer (see figures 9*a*i and 9*b*i). Along the curved section, I decreases with the amplification of $\overline{u'_\eta u'_\eta}$ and $\overline{w'w'}$ associated with the formation

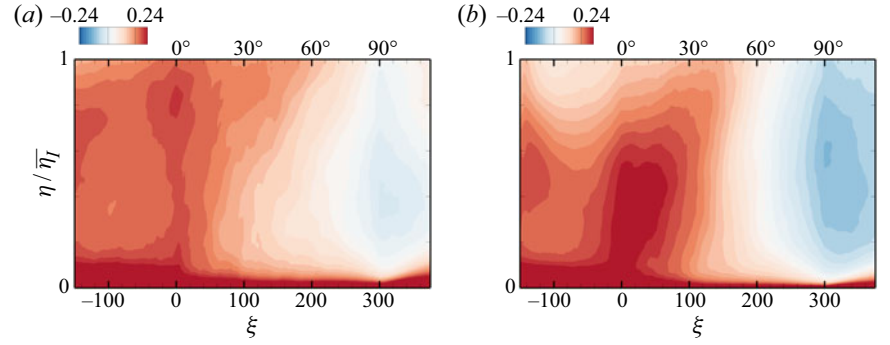

Figure 11. Deviation of Reynolds normal stresses from isotropy, $I = \overline{u'_\xi u'_\xi}/2k - 1/3$: (*a*) REF and (*b*) FRC.

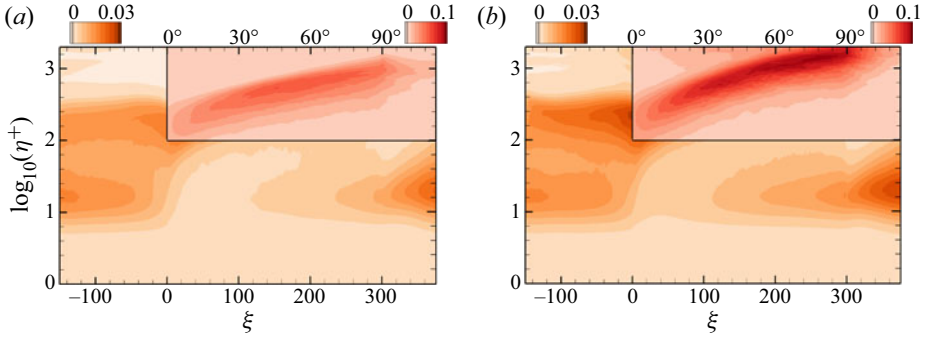

Figure 12. Contours of pre-multiplied TKE production, $\eta^+\mathcal{P}$: (*a*) REF and (*b*) FRC.

of outer Görtler structures. The decay in I is more precipitous in the forced flow in the region $50 \lesssim \xi \lesssim 300$, which is symptomatic of the larger amplification of these structures.

The changes in the normal stresses are paralleled by changes in the production of TKE, $\mathcal{P} = -\boldsymbol{R} : \boldsymbol{\nabla}\bar{\boldsymbol{u}}$, where $\boldsymbol{R}$ is the Reynolds stress tensor. In figure 12, since a logarithmic scale is adopted in the wall-normal direction, the contours show the pre-multiplied quantity $\eta^+\mathcal{P}$ in order to reflect the contribution to the wall-normal integral. Also note that two contour levels are adopted in each figure, with larger range for the outer region of the boundary layer above the curved surface. On the flat upstream section, the inner and outer peaks make comparable contributions to the integrated production, and both are enhanced by FST – an effect that has been detailed in previous studies (You & Zaki 2019). The APG at the flat-to-curved transition suppresses the near-wall production, and recovery is slow on the curved region, albeit faster in the presence of FST. In the outer region of the curved-wall boundary layer ($\xi \gtrsim 0$), the production peak is significantly enhanced. While its initial amplification near the onset of curvature coincides with the lifting of near-wall streaks due to APG, its continued amplification downstream coincides with the amplification of the outer stresses and potentially the formation and amplification of Görtler structures. In the presence of free-stream forcing, the magnitude of that outer peak is nearly twice its value in the reference configuration.

The TKE production in the outer region is significantly affected by Reynolds shear stresses. We first recall results from forced flat-plate boundary layers for comparison: even when the FST is isotropic, and hence free of average shear stress, it enhances $-\overline{u'_\xi u'_\eta}$

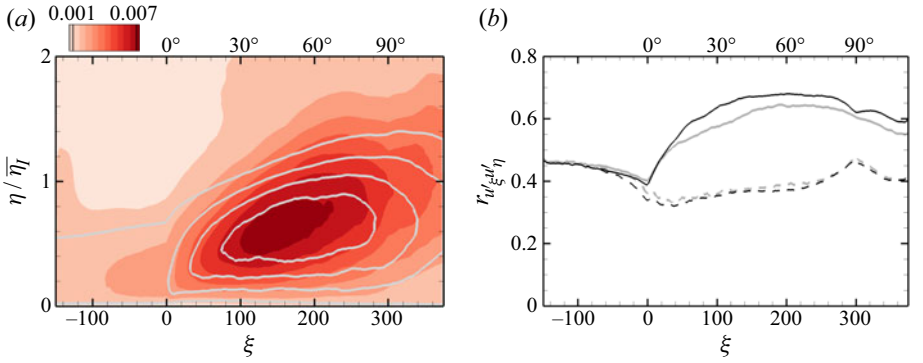

Figure 13. (*a*) Reynolds shear stress $-\overline{u'_\xi u'_\eta}$ for the REF (line) and FRC (colour) cases. Contour lines correspond to levels from 1×10^{-3} with increment 1×10^{-3}. (*b*) Downstream development of shear-stress correlation coefficient $r_{u'_\xi u'_\eta}$, extracted at $\eta^+ = 10$ (dashed line) and wall-normal location of the maximum (solid line), for REF (grey) and FRC (black).

within the boundary layer, although it reduces the stress correlation coefficient $r_{u'_\xi u'_\eta} \equiv -\overline{u'_\xi u'_\eta}/u'_{\xi,rms}u'_{\eta,rms}$ (Hancock & Bradshaw 1989; Thole & Bogard 1996). The shear stress and its correlation coefficient for the present curved-wall boundary layers are reported in figure 13. The former quantity is plotted throughout the boundary layer, and the latter is extracted at select locations. Over the curved section, $-\overline{u'_\xi u'_\eta}$ increases appreciably and reaches larger values for the FRC case. Figure 13(*b*) shows the correlation coefficient at $\eta^+ = 10$ and at the wall-normal height where it is maximum. The figure shows that the peak occurs at $\eta^+ = 10$ on the flat section of the wall, but the correlation at that location decays due to the pressure gradient (Gungor *et al.* 2016). Note that this effect was not reported in the previous experimental curved-wall studies by Barlow & Johnston (1988*a*), who removed the effect of the pressure gradient by contouring the top convex wall. On the curved wall, however, the peak shifts higher in the boundary layer and is much larger in magnitude because of the coherence of the turbulence structures in that region. In addition, the coefficient of the forced case is markedly greater in the outer region than that of the reference flow. We anticipate that the FST strengthens the outer roll motion on the curved region, thereby enhancing the correlation coefficient.

This section has demonstrated that the free-stream turbulent forcing mitigates the intermittent separation that can take place at the onset of curvature, enhances mixing of mean momentum along the curved wall and leads to appreciable and sustained increase in skin friction. The forcing also alters the state of the turbulence within the boundary layer along the curved wall. The distribution of the turbulent stresses suggests the formation of naturally triggered Görtler structures, which are more energetic and larger in size when the boundary layer is buffeted by the external turbulence. The following section upholds these interpretations by directly probing the flow structures on the curved wall without and with FST.

4. Modification of boundary-layer structures

A commonly adopted approach to identifying coherent vortical motions is to evaluate an invariant of the velocity gradient tensor, for example $Q \equiv \Omega_{ij}\Omega_{ij} - S_{ij}S_{ij}$ where S_{ij} is the symmetric, rate-of-deformation tensor and Ω_{ij} is the anti-symmetric, spin tensor. Figure 14 shows isosurfaces of the Q-criterion coloured by their wall-normal distance. In both REF

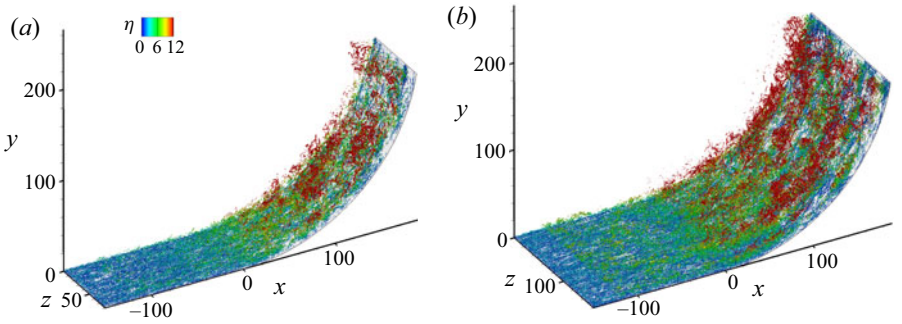

Figure 14. Isosurface of Q-criterion with threshold $Q = 0.03$, coloured by $0 \leq \eta \leq 12$: (*a*) REF and (*b*) FRC.

and FRC, the structures grow and spread in η as they travel into the concave curvature; similar observations have been made for FST-free flows (Arolla & Durbin 2015). This trend is consistent with the development of the outer peak in the profiles of Reynolds stresses (figure 9). The increase in vortical activity has previously been attributed to Görtler vortices due to the centrifugal effect, although coherent large-scale vortical structures are not apparent in the figure. It is also important to note that the response in the presence of FST is hardly distinguishable from the reference flow, based on the instantaneous Q isosurfaces. While streamwise organization is visually discernible in the figure, Görtler vortices, which are associated with coherent longitudinal roll motions, cannot be easily identified, and attempts to adopt filtering techniques were not successful.

Direct identification of naturally emerging Görtler motions in turbulent flows over curved walls is difficult. This challenge led Barlow & Johnston (1988*b*) to artificially impose them using vortex generators. For streamwise homogeneous flows, Moser & Moin (1987) performed streamwise averaging of the velocity field to visualize vortical structures in a curved channel flow. Due to streamwise inhomogeneity in the present configuration, however, we consider the Gaussian-filtered velocity fields, as done in previous studies (Hutchins & Marusic 2007; Lee *et al.* 2014; Hwang *et al.* 2016). The displacement of momentum effected by the Görtler motions generates coherent tangential velocity perturbations that are readily observable in the Gaussian-filtered $\hat{u}'_\xi$. Following the approach described by Lee *et al.* (2017), we evaluate isosurfaces of $\hat{u}'_\xi$ and identify the cores of those structures (see figure 15). In order to interpret the present results, it is helpful to recall those for a flat plate at the same Reynolds numbers (You & Zaki 2019). In that case, a canonical boundary layer without free-stream forcing does not develop outer large-scale motions; under FST, large-scale structures form and amplify, but a much longer streamwise extent is required than the flat region in the present configuration. Contrasting REF and FRC for $\xi < 0$, the velocity structures appear similar in that region, and hence any differences downstream on the curved wall are due to the interaction in that regime. There, the outer structures are clearly visible, and the isosurfaces are larger in the presence of free-stream forcing, which also implies that the tangential velocities within their cores are higher in amplitude.

Figure 15 also shows that we can identify the cores of the large-scale structures, which can be classified as positive $\mathcal{C}^P$ ($\hat{u}'_\xi > 0$) or negative $\mathcal{C}^N$ ($\hat{u}'_\xi < 0$). The p.d.f. of the lengths l_g of these cores is reported in the inset, for structures that are detected in the outer region $30 < \eta^+ < \eta_I^+$ at $\xi = 100$ ($\varphi = 30^\circ$). The p.d.f. shows an increased probability at lengths $O(5\text{–}6\,\delta_{99})$. In addition to their streamwise advection, these cores exhibit a weak spanwise

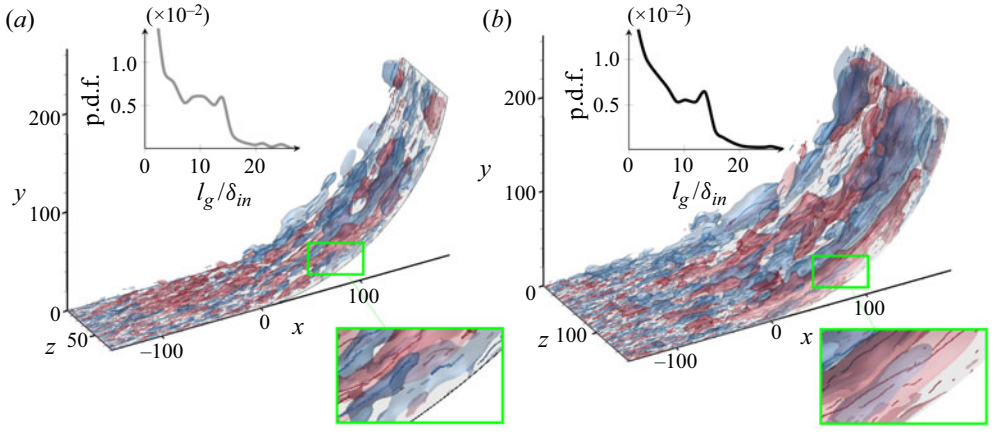

Figure 15. Isosurfaces of filtered streamwise velocity, $\hat{u}'_\xi = +0.06$ (red) and $\hat{u}'_\xi = -0.06$ (blue): (*a*) REF and (*b*) FRC. Lines within the transparent surfaces mark the cores of the structures. Insets show the p.d.f. of the lengths of the cores that are detected in the outer region $30 < \eta^+ < \eta_I^+$ and that cross $\xi = 100$ ($\varphi = 30^\circ$).

drift velocity with equal probability of positive or negative value. The average w along the core of a structure is typically one order of magnitude less than the local w'_{rms}.

Definitive evidence of the outer roll, or Görtler, motions and their influence on the near-wall flow are sought by computing conditionally averaged velocity perturbation fields. The condition adopted for averaging is the existence of a core of an outer tangential velocity structure, which is further differentiated into positive and negative ones as for the instantaneous visualization (cf. figure 15). The conditionally averaged perturbation fields are therefore

$$\boldsymbol{u}^P_{\mathcal{L}}(\Delta\xi, \eta, \Delta z) = \overline{\boldsymbol{u}(\xi_o + \Delta\xi, \eta, z + \Delta z)|\mathcal{C}^P}_{|30<\eta^+<\eta_I^+}, \tag{4.1}$$

$$\boldsymbol{u}^N_{\mathcal{L}}(\Delta\xi, \eta, \Delta z) = \overline{\boldsymbol{u}(\xi_o + \Delta\xi, \eta, z + \Delta z)|\mathcal{C}^N}_{|30<\eta^+<\eta_I^+}. \tag{4.2}$$

Figures 16 and 17 show the contours of $\boldsymbol{u}^P_{\mathcal{L}}$ and $\boldsymbol{u}^N_{\mathcal{L}}$, with the reference streamwise position $\xi_o = 100$ (30° station). Vectors represent the in-plane velocity components. While the outer roll motions are visible at $\Delta\xi = 0$ in the canonical boundary layer, they are much more pronounced (larger in size and amplitude) beneath FST. The more important observation, however, is the persistence of the roll motion and associated tangential velocity response upstream and downstream of the reference position. In the quiescent flow, the perturbation field $u'^{\{P,N\}}_{\xi\,\mathcal{L}}(\Delta\xi = \pm 25)$ is decorrelated appreciably from the reference point (e.g. figures 16 and 17, panels *a*i and *a*iii). In contrast, in the FRC case, the structures identified at the reference location persist beyond $\Delta\xi = \pm 25$ (e.g. figures 16 and 17, panels *b*i and *b*iii). The improved coherence underscores that FST does not decorrelate the turbulence within the logarithmic layer on the curved section, but rather promotes it.

The outer roll motion also increases in size with downstream distance, from $\Delta\xi = -25$ to $\Delta\xi = +25$. This view is also supported by further evidence (not shown) where we evaluated the conditional velocity fields using (4.1) and (4.2) at reference locations $\xi_o = 75$ and $\xi_o = 125$. The large roll motions which are growing with downstream distance in the forced flow are consistent with earlier statistical evidence based on the Reynolds stress, namely that the gap between the peaks of $\overline{u'_\eta u'_\eta}$ and $\overline{w'w'}$ increases along the curved wall (cf. figure 10).

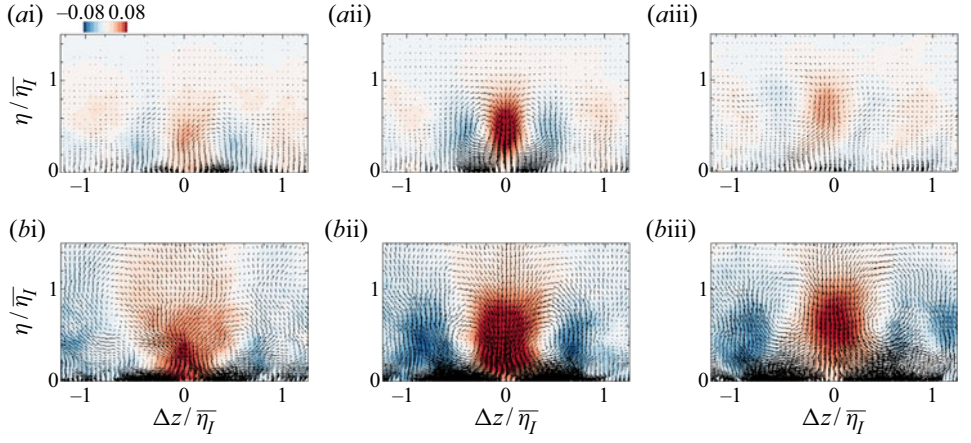

Figure 16. Conditionally averaged positive streamwise velocity on the curve with reference position $\xi_o = 100$ (30° station), and coloured by $u'^{P}_{\xi\mathcal{L}}$. Black vectors are $(u'^{P}_{\eta\mathcal{L}}, w'^{P}_{\mathcal{L}})$. (*a*) REF, (*b*) FRC; (i) $\Delta\xi = -25$, (ii) $\Delta\xi = 0$ and (iii) $\Delta\xi = +25$.

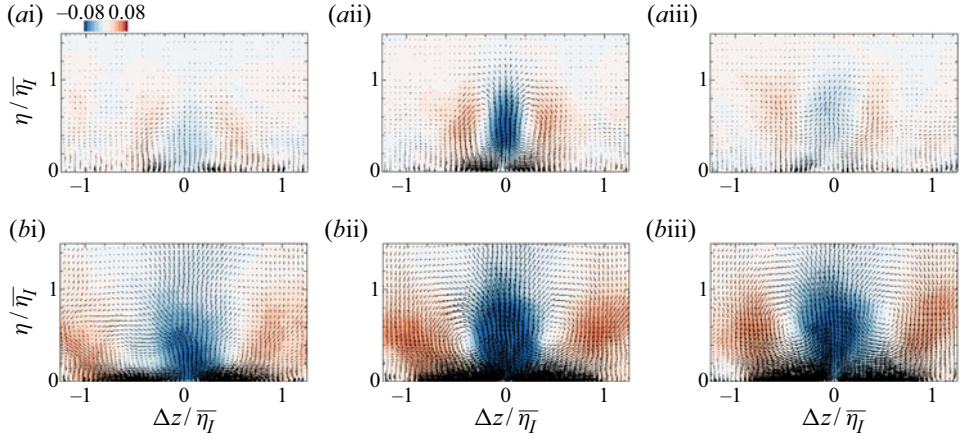

Figure 17. Conditionally averaged negative streamwise velocity on the curve with reference position $\xi_o = 100$ (30° station), and coloured by $u'^{N}_{\xi\mathcal{L}}$. Black vectors are $(u'^{N}_{\eta\mathcal{L}}, w'^{N}_{\mathcal{L}})$. (*a*) REF, (*b*) FRC; (i) $\Delta\xi = -25$, (ii) $\Delta\xi = 0$ and (iii) $\Delta\xi = +25$.

The amplification of Görtler motions depends on the stability characteristics of the boundary layer and the upstream forcing (Hall 1982). In the REF case, the forcing is provided solely by the turbulence in the upstream boundary layer, and an associated Görtler response develops on the curve. In the FRC case, there is the additional free-stream forcing which interacts with the developing boundary layer. As early as the flat section, the results of You & Zaki (2019) show that the low-frequency perturbations from the free stream are effective at penetrating the logarithmic layer. The APG which reduces shear sheltering can promote such penetration (Zaki & Durbin 2006). As a result, the dominant Görtler response on the curved section may differ from the REF case. We evaluate the spectra to examine the energy at different scales in the perturbation fields. Figure 18 shows

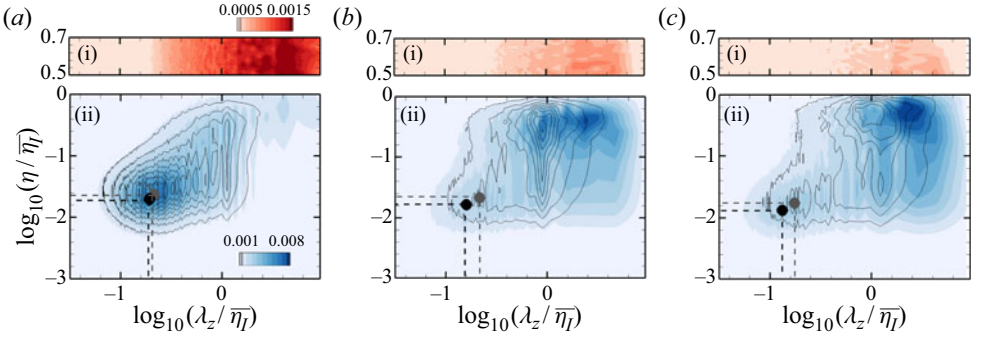

Figure 18. Pre-multiplied spanwise energy spectra at (*a*) $\xi = -100$, (*b*) $\xi = 50$ and (*c*) $\xi = 100$, with levels (i) $0.0005 \leq \kappa_z \Phi_{u'_\xi u'_\xi} \leq 0.0015$ in the free stream and (ii) $0.001 \leq \kappa_z \Phi_{u'_\xi u'_\xi} \leq 0.008$ in the boundary layer, for REF (black lines) and FRC (colour). Filled circles mark $\eta^+ = 10$ and $\lambda_z^+ = 100$ in REF (grey) and FRC (black).

the spanwise energy spectra of the streamwise velocity,

$$\Phi_{u'_\xi u'_\xi}(\lambda_z) = \int_{-\infty}^{\infty} \overline{u'_\xi(z) u'_\xi(z+\zeta)} \mathrm{e}^{-\mathrm{i}\kappa_z \zeta} \, \mathrm{d}\zeta, \tag{4.3}$$

pre-multiplied by spanwise wavenumber $\kappa_z = 2\pi/\lambda_z$, where λ_z is the wavelength. Three streamwise positions are considered, and at each the spectrum is reported (i) in the free stream and (ii) within the boundary layer, where line and colour contours correspond to the REF case and the FRC case, respectively. On the flat section (figure 18*a*), only an inner peak is visible, be that in the REF or the FRC boundary layer. A faint increase of energy is observed near the edge of the FRC boundary layer at large spanwise scales that are commensurate with the most energetic wavelengths in the free stream in (*a*i). On the curved section, the energy in the small wavelengths decreases (figure 18*b*,*c*), which is consistent with reduced TKE dissipation (not shown). In the reference flow, a clear outer peak emerges at $\lambda_z \approx \overline{\eta_I}$. In contrast, in FRC at 15° (colour contour of figure 18*b*), there are two outer peaks, and both are associated with Görtler motions. The first, at the smaller spanwise wavelength (left), coincides with the contours of the canonical boundary layer and corresponds to the naturally forming Görtler vortices. The second emerges at the wavelength of the free-stream turbulent forcing (see panel (*a*i)); this peak is the boundary-layer Görtler response to the external forcing. The two peaks ultimately merge downstream at $\xi = 100$, with the larger Görtler vortices becoming dominant. As in earlier studies of turbulence on curved walls (Tani 1962), comparison can be made to results from linear stability. In our configuration, at $\xi = 50$, the local Görtler number is $G_t = 5.4$ (cf. figure 5*b*), and the most energetic spanwise wavenumber is $\kappa_z \theta = 0.43$, which is also the most unstable mode according to linear theory (Smith 1955; Tani 1962). An important observation is the extent to which that wavenumber persists, or remains energetic, deep into the boundary layer, which is suggestive of a stronger modulation of the near-wall region than in flat plates, perhaps even a direct influence.

The small-scale energy in the near-wall region is also modified by the free-stream forcing. Figure 18 shows that, along the curved wall, energy shifts towards smaller spanwise wavenumbers in FRC, which is consistent with enhanced dissipation. The inner peak in the spectra is generally located at $\eta^+ \approx 10$ and $\lambda_z^+ \approx 100$, and thus the downstream dependence of $\kappa_z \Phi_{u'_\xi u'_\xi}$ at the position is provided in figure 19. Downstream of the fast

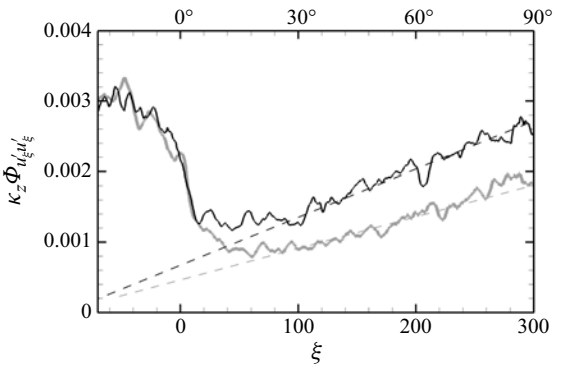

Figure 19. Downstream development of $\kappa_z \Phi_{u'_\xi u'_\xi}$ at $\eta^+ = 10$ and $\lambda_z^+ = 100$: REF (grey) and FRC (black). Dashed lines indicate the recovery rate in Region 2.

decay associated with the APG at the onset of curvature, $\kappa_z \Phi_{u'_\xi u'_\xi}$ recovers at a faster rate for FRC.

The coherent outer Görtler motions have important implications, including their ability to enhance mixing and, in the forced configuration, potentially transport the FST deep into the boundary layer towards the wall. An objective measure of penetration of the free-stream fluid into the boundary layer is the intermittency γ. Starting from the level-set function, which provides an objective instantaneous virtual interface between the two regions, an indicator function is defined as $\Gamma = \{0, 1\}$ for $\psi \gtrless 0.5$, and then averaged to obtain $\gamma = \bar{\Gamma}$. We recall that in a flat-plate boundary layer, You & Zaki (2019) adopted the same measure and demonstrated that the FST does not breach the buffer layer within the streamwise domain length of interest here. The results for the present curved-wall configuration are reported in figure 20. Figure 20(*a*) captures the difference between the flat and curved sections: even for the unforced flow the intermittency isolines spread more quickly on the curve, which is indicative of enhanced mixing of the free-stream and boundary-layer fluids (see also the wall-normal profiles in outer scaling in figure 20*b*). Forcing by FST amplifies these trends significantly, and in panels (*c*iii–iv) we observe remarkable levels of penetration of FST inside the buffer layer at $\xi \gtrsim 100$ ($\varphi > 30°$, Region 2). This enhanced 'mixing' is unique to the present configuration and is precipitated by the large-scale outer roll motions, which transport the free-stream fluid deep towards the wall and eject near-wall fluid outward. The interaction of the outer and inner regions is therefore direct. Ultimately, however, this large-scale effect is also accompanied by further dispersion of the ingested turbulence due to the various flow scales within the boundary layer, and by molecular diffusion acting on the smallest scales. Thus, we next consider the recovery of the near-wall small-scale structures on the curved wall, and in particular their modulation by the outer large scales that can spur that recovery.

Bernardini & Pirozzoli (2011) defined the two-point amplitude modulation (AM) coefficient $C_{u_\xi, u_\xi}(\eta_1, \eta_2)$ in order to quantify the influence of the large-scale motion at η_1 on the near-wall motion at η_2, where

$$C_{u_\xi, u_\xi}(\eta_1, \eta_2) = \overline{u_\xi{}'_L(\eta_1) u_\xi{}'_{EL}(\eta_2)}, \tag{4.4}$$

$u_\xi{}'_L$ is a large-scale velocity and $u_\xi{}'_{EL}$ is a filtered envelope of a small-scale part. The cut-off filter for the large- and small-scale signal is set to $0.5\overline{\eta_I}$, which from the spectra shown in figure 18 should discriminate between these scales. In the flat section ($\xi = -100$),

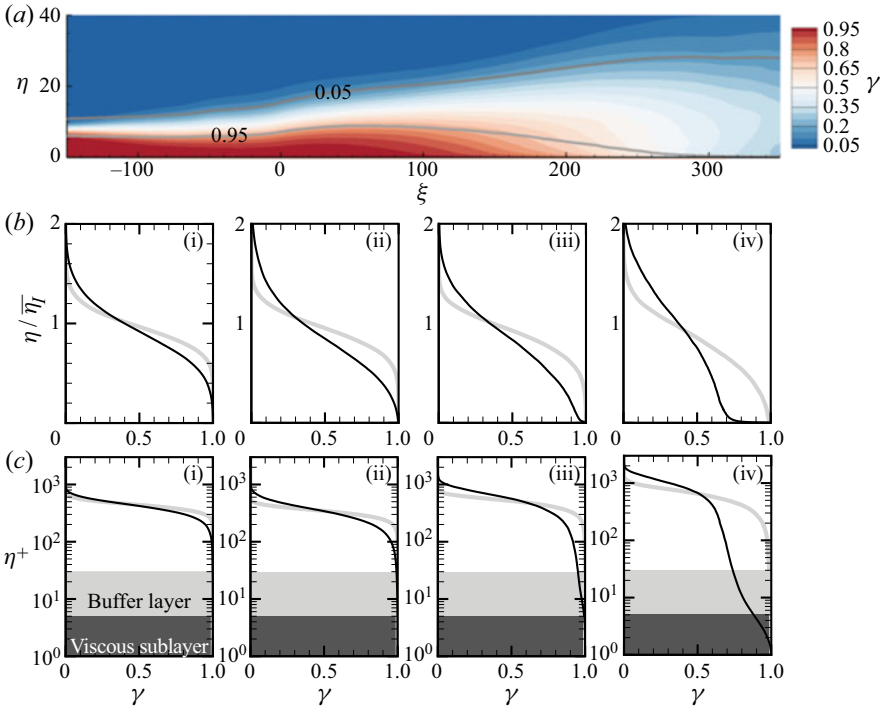

Figure 20. (*a*) Intermittency γ for REF (lines, $\gamma = \{0.05, 0.95\}$) and FRC (colour, $0.05 \leq \gamma \leq 0.95$). Intermittency profiles in (*b*) outer and (*c*) viscous units, at (i) $\xi = -100$,(ii) $\xi = 0$, (iii) $\xi = 100$ and (iv) $\xi = 200$: REF (grey) and FRC (black).

figure 21(i) shows that the upstream boundary layer exhibits a weak level of modulation beneath a quiescent free stream, and this effect is enhanced under FST. In the latter case, the outer large-scale motions at $\eta_1^+ \approx 100$ show relatively higher levels of modulation of the small scales at $\eta_2^+ \approx 7$. These results are typical of flat plates, and the values of $C_{u_\xi,u_\xi}(\eta_1, \eta_2)$ would increase downstream if the flat section were extended. A qualitative change takes place over the curved section: figure 21(ii) highlights a much stronger modulation (note the change in the contour levels), especially in the forced flow, where the coefficient at $(\eta_1^+, \eta_2^+) \approx (100, 7)$ is now dominant and is nearly twice as high as in the case without FST. The results for FRC are the outcome of the energetic footprint of the large scales that persists near the wall (figure 18) and leads to a faster recovery of near-wall small scales (see figure 19).

The deep ingestion of outer fluid by the Görtler structures not only modulates the near-wall scales but also influences the stress at the wall, which is of practical interest. In order to empirically demonstrate this connection, figure 22(i) shows an instantaneous realization of the skin-friction coefficient c_f, and figure 22(ii) show the corresponding tangential velocity fluctuations u'_ξ in the outer region. The contours of c_f initially have a streaky pattern that is disrupted by the APG at the onset of curvature. However, the most important observation is downstream, where localized large-scale regions of high c_f are observed on the curved wall beneath outer large-scale and high-amplitude u'_ξ perturbations.

Close inspection of figure 22(i) also provides visual support of faster recovery of the small-scale near-wall structures. For both REF and FRC, the streamwise-aligned near-wall

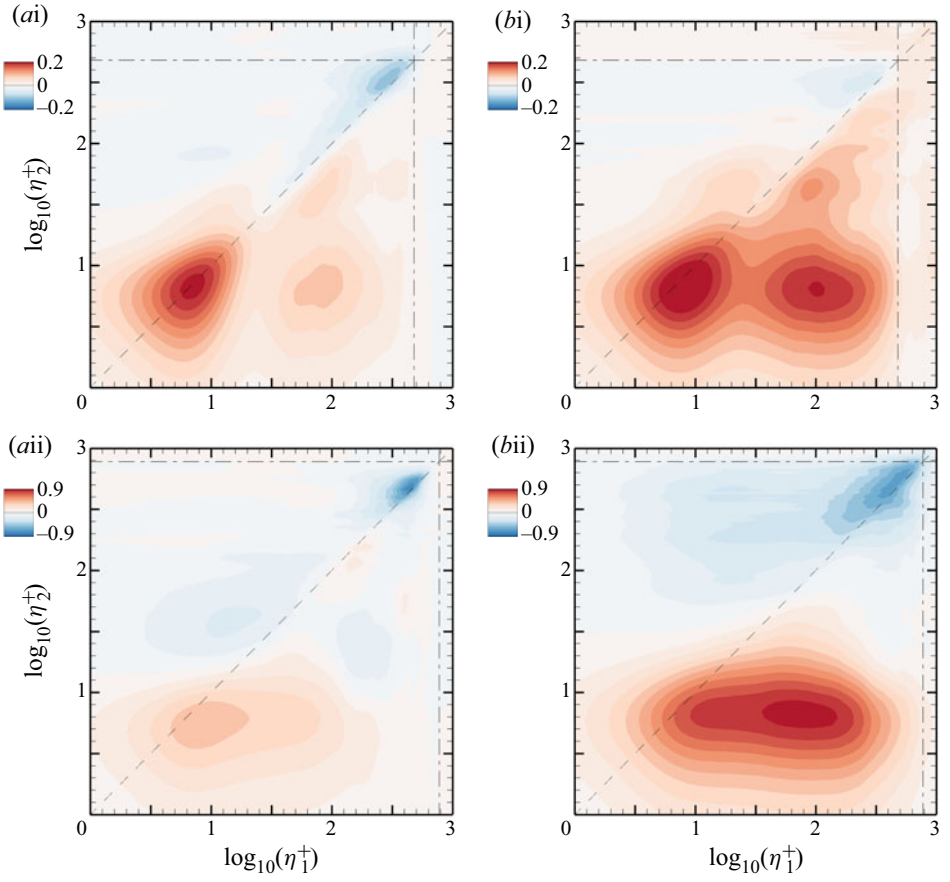

Figure 21. Amplitude-modulation coefficient $C_{u_\xi,u_\xi}/u_\tau^2$ for (*a*) REF and (*b*) FRC. (i) Flat section ($\xi = -50$); (ii) curved section ($\xi = 100$; 30° station). Vertical and horizontal dash-dotted lines mark the edge of the boundary layer, $\eta = \overline{\eta_I}$.

streaks have an intense signature in the wall stress on the flat plate, which is abruptly disrupted near the onset of curvature $\xi \approx 0$. The re-emergence of this signature across the span is clear near the end of the curved wall, $\xi \approx 300$. The key observation, however, is that FST re-establishes these streaky structures much earlier upstream on the curve, albeit intermittently, as early as $\xi \approx 50$ for this particular flow realization.

The above empirical observations are quantified, first using the normalized two-point correlation of the wall stress in the span,

$$R_{\tau_w\tau_w}(\xi, \Delta z) = \frac{\overline{\tau_w(\xi, z)\tau_w(\xi, z + \Delta z)}}{\overline{\tau_w(\xi, z)\tau_w(\xi, z)}}. \tag{4.5}$$

Figure 23(*a*) shows that, on the flat section ($\xi = -100$), the wall stress τ_w decorrelates within a fraction of the boundary-layer thickness. In contrast, on the curve, the stress is much more correlated in the span, and the correlation length is much wider in the presence of free-stream forcing, potentially because of the larger size of the outer Görtler motions.

Here we examine whether the wall stress beneath the outer roll motions is indeed statistically large in scale and magnitude, not only in a single realization as shown in

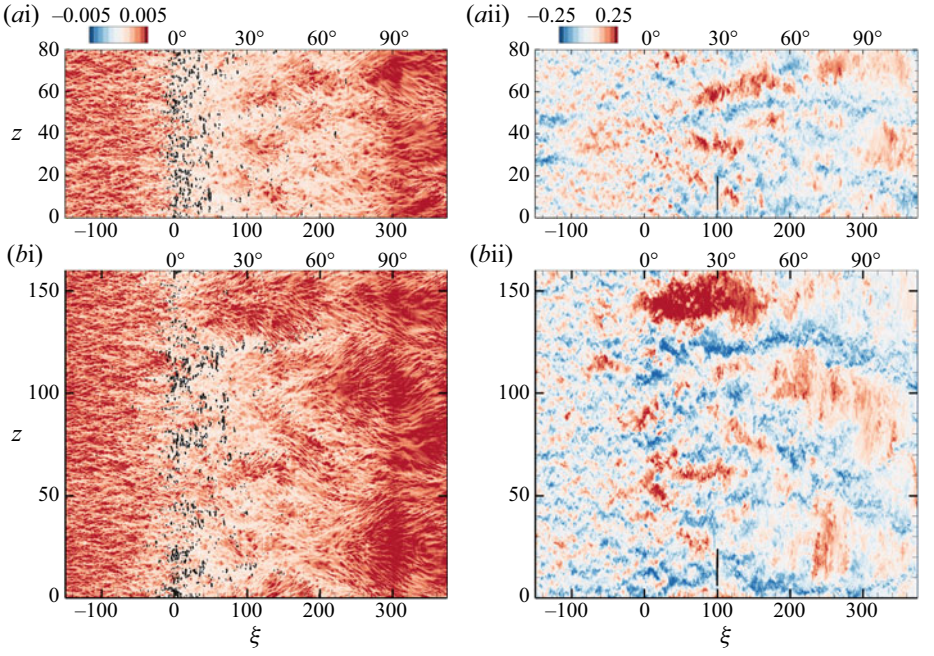

Figure 22. (i) Top view of instantaneous skin-friction coefficient, $-0.005 \leq c_f \leq 0.005$, and black isocontour marks $c_f = 0$. (ii) Instantaneous streamwise-velocity fluctuations $-0.25 \leq u'_\xi \leq 0.25$ at $\eta \approx 3$ ($\eta^+ \approx 100$ at $\xi = 0$). (*a*) REF; (*b*) FRC. The short black line in (ii) is a graphical length scale equal to $\overline{\eta_I}$ at $\xi = 100$.

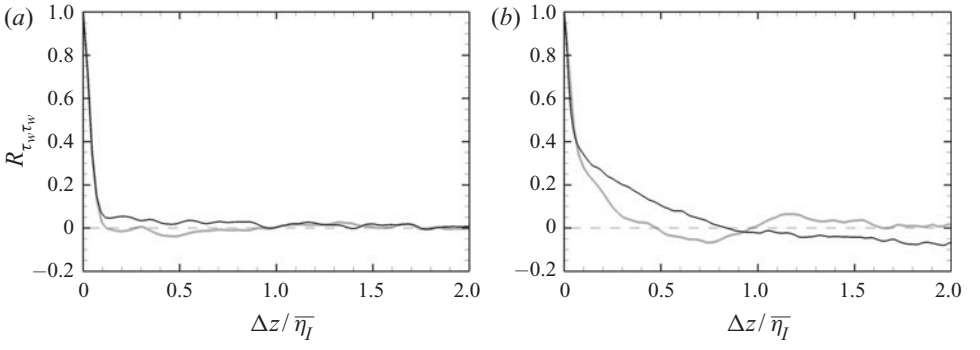

Figure 23. Spanwise two-point correlation of the wall-shear stress $R_{\tau_w\tau_w}$ at (*a*) $\xi = -100$ and (*b*) $\xi = 100$ (30° station): REF (grey) and FRC (black).

figure 22 but in a statistically significant fashion. This point is upheld by direct evaluation of the average perturbation wall stress,

$$c_f^P(\Delta\xi, \Delta z) = \overline{c'_f(\xi + \Delta\xi, z + \Delta z)|\mathcal{C}^P}_{|30<\eta^+<\eta_I^+} \tag{4.6}$$

and

$$c_f^N(\Delta\xi, \Delta z) = \overline{c'_f(\xi + \Delta\xi, z + \Delta z)|\mathcal{C}^N}_{|30<\eta^+<\eta_I^+}, \tag{4.7}$$

conditional on the presence of an outer large-scale tangential velocity structure as a surrogate for the Görtler structures. The results are reported in figure 24. In both the

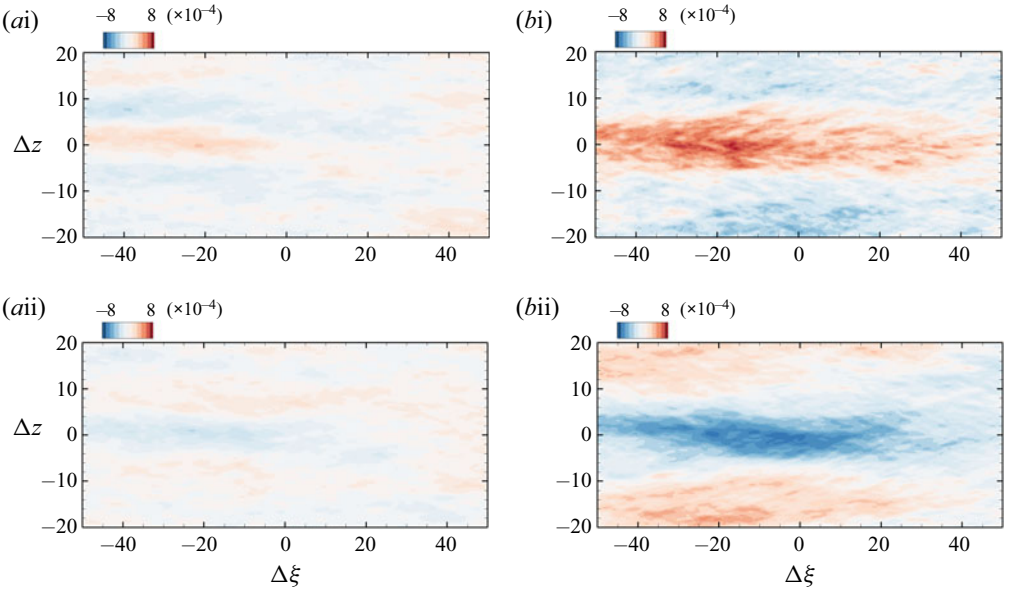

Figure 24. Conditionally averaged skin-friction coefficient from (*a*) REF and (*b*) FRC at $\xi = 100$ (30° station): (i) $|c_f^P| \leq 8 \times 10^{-4}$ and (ii) $|c_f^N| \leq 8 \times 10^{-4}$.

REF and FRC flows, the peak perturbation stresses are recorded at $\Delta\xi < 0$, which is consistent with an inclination of the outer structures relative to the wall. However, in the forced case, the magnitude of perturbations in the wall stress is larger, and the footprint of the outer large scales is greater in extent. In fact, the affected region extends over a longer streamwise distance $\Delta\xi$ (both positive and negative $\Delta\xi$) due to the coherence of the outer large scales in this case (cf. figures 16 and 17). In addition, the opposite wall stress perturbations are observed in the span, which is consistent with the influence of roll motions displacing momentum away from and towards the wall at spanwise locations that are separated by their width.

The results presented here provide a structural interpretation of the statistical changes of the boundary layer on the curved surface, without and with FST. While Görtler structures may be elusive in the former case, they are more prominent in the forced flow. Their higher amplitude, larger size and strong coherence are evident in the spectra and in conditional averages. The more energetic Görtler structures also promote the recovery of the boundary layer downstream of the APG at the onset of curvature, increase mixing in the wall-normal direction and appreciably enhance the wall stress in their footprint.

5. Conclusion

We have contrasted direct numerical simulations of TBLs on a concave curve without and with FST. In the latter case, the inlet turbulence was homogeneous and isotropic with intensity $Tu = 10\,\%$. The boundary layer and the FST were differentiated using a level-set approach which provides an objective, virtual interface.

Near the onset of the curvature, the drag drops significantly on account of the APG, which induces intermittent flow separation. The forcing by FST reduces the probability of separation and promotes the downstream recovery of the flow along the ZPG section of the curve. The external forcing also increases the skin friction by up to 49% relative to the reference flow (figure 6).

The curved wall has a clear impact on the wall-normal and spanwise normal stresses, both indicative of the development of Görtler vortices in the outer region (figure 9). The wall-normal separation between the peaks of these components of stress increases with downstream distance, signalling the growth of the vortices as the boundary layer expands (figure 10). When FST is present, the outer roll motions are more energetic and larger in size. In addition, and in contrast to the case of flat-plate boundary layers, introducing FST increases the peak shear-stress correlation coefficient in the curved-wall flow (figure 13*b*).

Above the curved section, the turbulence structures are significantly modified. Curvature spurs the formation of outer roll motions which increase in size on the concave wall, as seen in the conditionally averaged flow fields (figures 16 and 17). In the forced flow, these longitudinal structures, which we interpret as Görtler vortices, are enlarged in size and strengthened in intensity, and they display a clear streamwise coherence and enhanced wall-normal mixing. As a result, the probability of observing free-stream fluid remains finite within the buffer layer (figure 20), in contrast to earlier results for flat-plate boundary layers, where external turbulence could not reach the buffer layer (You & Zaki 2019). The impact on the near-wall region is direct (figure 21), in particular in the wall stress at their footprint (figure 24).

Funding. This work is sponsored by the National Science Foundation (grant 1605404). Computational resources were provided by the Maryland Advanced Research Computing Center (MARCC).

Declaration of interests. The authors report no conflict of interest.

Author ORCIDs.
David A. Buchta https://orcid.org/0000-0002-7068-6226;
Tamer A. Zaki https://orcid.org/0000-0002-1979-7748.

Appendix A. The momentum thickness

The momentum thickness is an important proxy of the state of the boundary layer. Various definitions have been proposed for curved-wall flows, and we here consider the form adopted by Patel (1969),

$$\theta = \int_0^{\eta_p} \frac{\overline{u_\xi}}{U_{pw,R}} \left(\frac{U_{p,R}}{U_{pw,R}} - \frac{\overline{u_\xi}}{U_{pw,R}} \right) \mathrm{d}\eta. \tag{A1}$$

The subscript R indicates that we are adopting the profile of the potential velocity from the REF case, which is not necessarily preserved in the FRC case. For this reason, we also perform the integration up to the wall-normal position η_p where the potential-velocity profiles from both REF and FRC intersect. The downstream dependence of θ is reported in figure 25(*a*), which shows the anticipated increase in the momentum thickness near $\xi = 0$ due to flow deceleration. On the curved wall θ is larger in the FRC case; this effect is seemingly consistent with results on flat-plate boundary layers, where the change in θ can be directly related to increase in skin friction under FST forcing. The reality, however, is more complex, as can be shown by re-expressing the momentum thickness as follows:

$$\theta = \frac{(U_{pw})^2}{(U_{pw,R})^2} \underbrace{\int_0^{\eta_p} \frac{\overline{u_\xi}}{U_{pw}} \left(\frac{U_p}{U_{pw}} - \frac{\overline{u_\xi}}{U_{pw}} \right) \mathrm{d}\eta}_{=\tilde{\theta}} + \int_0^{\eta_p} \frac{\overline{u_\xi}}{U_{pw,R}} \left(\frac{U_{p,R}}{U_{pw,R}} - \frac{U_p}{U_{pw,R}} \right) \mathrm{d}\eta. \tag{A2}$$

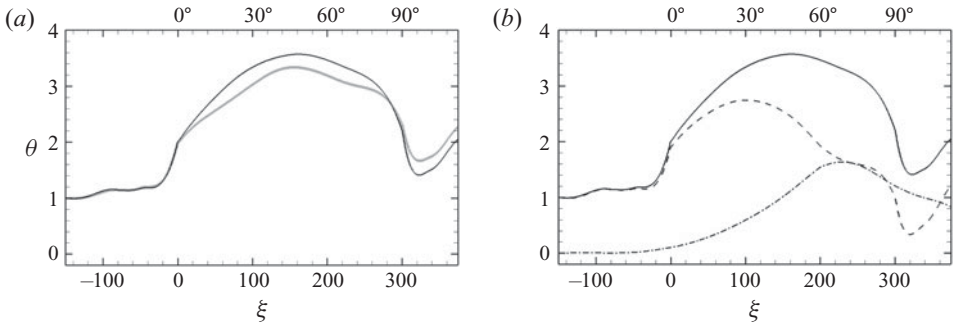

Figure 25. (*a*) Development of momentum thickness θ in REF (grey) and FRC (black). (*b*) For FRC, θ (black solid line) is further decomposed into the two contributions (black dashed line and black dash-dotted line) on the right-hand side of (A2).

The first term involves a momentum thickness $\tilde{\theta}$ defined using the potential velocity of each flow (instead of adopting $U_{p,R}$ for both REF and FRC), and the second term is due to the difference of the potential velocities in the two simulations. Figure 25(*b*) shows that the increase in θ in FRC is due to this second term. The thicker boundary layer in the forced case increases the effective curvature, specifically $\overline{\eta_I}/R$ or similarly δ_{99}/R, and hence the turning of the outer flow. The result is a steeper U_p profile in the free stream, a lower U_p inside the boundary layer and increased deficit $U_{p,R} - U_p$. Interpretation of the momentum thickness must therefore take this effect into account.

References

Ames, F.E. & Moffat, R.J. 1990 Heat transfer with high intensity, large scale turbulence: the flat plate turbulent boundary layer and the cylindrical stagnation point. Stanford University Report No. HMT-44.

Arolla, S.K. & Durbin, P.A. 2015 LES of spatially developing turbulent boundary layer over a concave surface. *J. Turbul.* **16** (1), 81–99.

Bandyopadhyay, P.R. & Ahmed, A. 1993 Turbulent boundary layers subjected to multiple curvatures and pressure gradients. *J. Fluid Mech.* **246**, 503–527.

Barlow, R.S. & Johnston, J.P. 1988*a* Structure of a turbulent boundary layer on a concave surface. *J. Fluid Mech.* **191**, 137–176.

Barlow, R.S. & Johnston, J.P. 1988*b* Local effects of large-scale eddies on bursting in a concave boundary layer. *J. Fluid Mech.* **191**, 177–195.

Bernardini, M. & Pirozzoli, S. 2011 Inner/outer layer interactions in turbulent boundary layers: a refined measure for the large-scale amplitude modulation mechanism. *Phys. Fluids* **23**, 061701.

Castro, I.P. 1984 Effects of free-stream turbulence on low Reynolds number boundary layers. *Trans. ASME: J. Fluids Engng* **106**, 298–306.

Dogan, E., Hanson, R.E. & Ganapathisubramani, B. 2016 Interactions of large-scale free-stream turbulence with turbulent boundary layers. *J. Fluid Mech.* **802**, 79–107.

Floryan, J.M. 1991 On the Görtler instability of boundary layers. *Prog. Aerosp. Sci.* **28** (3), 235–271.

Gungor, A.G., Maciel, Y., Simens, M.P. & Soria, J. 2016 Scaling and statistics of large-defect adverse pressure gradient turbulent boundary layers. *Intl J. Heat Fluid Flow* **59**, 109–124.

Hall, P. 1982 Taylor–Gortler vortices in fully developed or boundary-layer flows: linear theory. *J. Fluid Mech.* **124**, 475–494.

Hancock, P.E. & Bradshaw, P. 1983 The effect of free-stream turbulence on turbulent boundary layers. *Trans. ASME: J. Fluids Engng.* **105**, 284–289.

Hancock, P.E. & Bradshaw, P. 1989 Turbulence structure of a boundary layer beneath a turbulent free stream. *J. Fluid Mech.* **205**, 45–76.

Harun, Z., Monty, J.P., Mathis, R. & Marusic, I. 2013 Pressure gradient effects on the large-scale structure of turbulent boundary layers. *J. Fluid Mech.* **715**, 477–498.

Hearst, R.J., Dogan, E. & Ganapathisubramani, B. 2018 Robust features of a turbulent boundary layer subjected to high-intensity free-stream turbulence. *J. Fluid Mech.* **851**, 416–435.

HICKEL, S. & ADAMS, N.A. 2008 Implicit LES applied to zero-pressure-gradient and adverse-pressure-gradient boundary layer turbulence. *Intl J. Heat Fluid Flow* **29**, 626–639.
HOFFMANN, P.H., MUCK, K.C. & BRADSHAW, P. 1985 The effect of concave surface curvature on turbulent boundary layers. *J. Fluid Mech.* **161**, 371–403.
HUNT, J.C.R. & DURBIN, P.A. 1999 Perturbed vortical layers and shear sheltering. *Fluid Dyn. Res.* **24** (6), 375–404.
HUTCHINS, N. & MARUSIC, I. 2007 Evidence of very long meandering features in the logarithmic region of turbulent boundary layers. *J. Fluid Mech.* **579**, 1–28.
HWANG, J., LEE, J., SUNG, H.J. & ZAKI, T.A. 2016 Inner-outer interactions of large-scale structures in turbulent channel flow. *J. Fluid Mech.* **790**, 128–157.
JELLY, T.O., JUNG, S.Y. & ZAKI, T.A. 2014 Turbulence and skin friction modification in channel flow with streamwise-aligned superhydrophobic surface texture. *Phys. Fluids* **26**, 095102.
JUNG, S.Y. & ZAKI, T.A. 2015 The effect of a low-viscosity near-wall film on bypass transition in boundary layers. *J. Fluid Mech.* **772**, 330–360.
KESTORAS, M.D. & SIMON, T.W. 1995 Effects of free-stream turbulence intensity on a boundary layer recovering from concave curvature effects. *Trans. ASME: J. Turbomach.* **117**, 240–247.
KESTORAS, M.D. & SIMON, T.W. 1998 Conditionally sampled measurements in a heated turbulent boundary layer: curvature and free-stream turbulence effects. *Exp. Therm. Fluid Sci.* **17**, 63–70.
KOZUL, M., HEARST, R.J., MONTY, J.P., GANAPATHISUBRAMANI, B. & CHUNG, D. 2020 Response of the temporal turbulent boundary layer to decaying free-stream turbulence. *J. Fluid Mech.* **896**, A11.
LEE, J., LEE, J.H., CHOI, J.-I. & SUNG, H.J. 2014 Spatial organization of large-and very-large-scale motions in a turbulent channel flow. *J. Fluid Mech.* **749**, 818–840.
LEE, J., SUNG, H.J. & ZAKI, T.A. 2017 Signature of large-scale motions on turbulent/non-turbulent interface in boundary layers. *J. Fluid Mech.* **819**, 165–187.
LIGHTHILL, M.J. 1963 *Boundary Layer Theory*. Oxford University Press.
LOPES, A.S., PIOMELLI, U. & PALMA, J.M.L.M. 2006 Large-eddy simulation of the flow in an *s*-duct. *J. Turbul.* **7** (11), 1–24.
LUND, T.S. & MOIN, P. 1996 Large-eddy simulation of a concave wall boundary layer. *Intl J. Heat Fluid Flow* **17**, 290–295.
MATHIS, R., HUTCHINS, N. & MARUSIC, I. 2009 Large-scale amplitude modulation of the small-scale structures in turbulent boundary layers. *J. Fluid Mech.* **628**, 311–337.
MOSER, R.D. & MOIN, P. 1987 The effects of curvature in wall-bounded turbulent flows. *J. Fluid Mech.* **175**, 479–510.
MOTOORI, Y. & GOTO, S. 2019 Generation mechanism of a hierarchy of vortices in a turbulent boundary layer. *J. Fluid Mech.* **865**, 1085–1109.
PATEL, V.C. 1969 *The Effects of Curvature on the Turbulent Boundary Layer*. Aeronautical Research Council, Report & Memoranda No. 3599.
PATEL, V.C. & SOTIROPOULOS, F. 1997 Longitudinal curvature effects in turbulent boundary layers. *Prog. Aerosp. Sci.* **33**, 1–70.
ROSENFELD, M., KWAK, D. & VINOKUR, M. 1991 A fractional step solution method for the unsteady incompressible Navier–Stokes equations in generalized coordinate systems. *J. Comput. Phys.* **94**, 102–137.
SARIC, W.S. 1994 Görtler vortices. *Annu. Rev. Fluid Mech.* **26** (1), 379–409.
SCHRADER, L.U., BRANDT, L. & ZAKI, T.A. 2011 Receptivity, instability and breakdown of Görtler flow. *J. Fluid Mech.* **682**, 362–396.
SIMONICH, J.C. & BRADSHAW, P. 1978 Effect of free-stream turbulence on heat transfer through a turbulent boundary layer. *Trans. ASME: J. Heat Transfer* **100**, 671–677.
SMITH, A.M.O. 1955 On the growth of Taylor–Görtler vortices along highly concave walls. *Q. Appl. Maths* **13** (3), 233–262.
TANI, I. 1962 Production of longitudinal vortices in the boundary layer along a concave wall. *J. Geophys. Res.* **67**, 3075–3080.
THOLE, K.A. & BOGARD, D.G. 1995 Enhanced heat transfer and shear stress due to high free-stream turbulence. *Trans. ASME: J. Turbomach.* **117**, 418–424.
THOLE, K.A. & BOGARD, D.G. 1996 High freestream turbulence effects on turbulent boundary layers. *Trans. ASME: J. Fluids Engng* **118**, 276–284.
THOMPSON, J.F., WARSI, Z.U.A. & MASTIN, C.W. 1985 *Numerical Grid Generation: Foundations and Applications*. North Holland.
WANG, M., WANG, Q. & ZAKI, T.A. 2019 Discrete adjoint of fractional-step incompressible Navier–Stokes solver in curvilinear coordinates and application to data assimilation. *J. Comput. Phys.* **396**, 427–450.
YOU, J. & ZAKI, T.A. 2019 Conditional statistics and flow structures in turbulent boundary layers buffeted by free-stream disturbances. *J. Fluid Mech.* **866**, 526–566.

YOU, J. & ZAKI, T.A. 2020 Turbulent heat-transfer enhancement in boundary layers exposed to free-stream turbulence. *Flow Turbul. Combust.* **104** (2), 381–402.

ZAKI, T.A. & DURBIN, P.A. 2006 Continuous mode transition and the effects of pressure gradient. *J. Fluid Mech.* **563**, 357–388.

ZAKI, T.A. & SAHA, S. 2009 On shear sheltering and the structure of vortical modes in single- and two-fluid boundary layers. *J. Fluid Mech.* **626**, 111–147.

ZAKI, T.A., WISSINK, J.G., RODI, W. & DURBIN, P.A. 2010 Direct numerical simulations of transition in a compressor cascade: the influence of free-stream turbulence. *J. Fluid Mech.* **665**, 57–98.